

Multiscale Processes and Nonlinear Dynamics of the Circulation and Upwelling Events off Monterey Bay

X. SAN LIANG

School of Engineering and Applied Sciences, Harvard University, Cambridge, Massachusetts, and State Key Laboratory of Satellite Ocean Environment Dynamics, Hangzhou, China

ALLAN R. ROBINSON

Department of Earth and Planetary Science and School of Engineering and Applied Sciences, Harvard University, Cambridge, Massachusetts

(Manuscript received 15 November 2007, in final form 18 July 2008)

ABSTRACT

The nonlinear multiscale dynamics of the Monterey Bay circulation during the Second Autonomous Ocean Sampling Network (AOSN-II) Experiment (August 2003) is investigated in an attempt to understand the complex processes underlying the highly variable ocean environment of the California coastal region. Using a recently developed methodology, the localized multiscale energy and vorticity analysis (MS-EVA) and the MS-EVA-based finite-amplitude hydrodynamic instability theory, the processes are reconstructed on three mutually exclusive time subspaces: a large-scale window, a mesoscale window, and a submesoscale window. The ocean is found to be most energetic in the upper layers, and the temporal mesoscale structures are mainly trapped above 200 m. Through exploring the nonlinear window–window interactions, it is found that the dynamics underlying the complex surface circulation is characterized by a well-organized, self-sustained bimodal instability structure: a Bay mode and a Point Sur mode, which are located near Monterey Bay and west of Point Sur, respectively. Both modes are of mixed types, but they are distinctly different in dynamics. The former is established when the wind relaxes, while the latter is directly driven by the wind. Either way, the wind instills energy into the ocean, which is stored within the large-scale window and then released to fuel temporal mesoscale processes. Upon wind relaxation, the generated mesoscale structures propagate northward along the coastline, in a form with dispersion properties similar to that of a free thermocline-trapped coastal-trapped wave. Between these two modes, a secondary instability is identified in the surface layer during 15–21 August, transferring energy to the temporal submesoscale window. Also studied is the deep-layer flow, which is unstable all the time throughout the experiment within the Bay and north of the deep canyon. It is observed that the deep temporal mesoscale flow within the Bay may derive its energy from the submesoscale window as well as from the large-scale window. This study provides a real ocean example of how secondary upwelling can be driven by winds through nonlinear instability and how winds may excite the ocean via an avenue distinctly different from the classical paradigms.

1. Introduction

Monterey Bay is a crescent-shaped large embayment indented on the central California coast (Fig. 1). Distinguished by its high productivity and marine life diversity, it has become an important arena of interdisciplinary research. Oceanographers began to show interest in this area as early as 1930 (Bigelow and Leslie

1930). Since then, continuing efforts have been invested to understand its circulation and dynamical processes, both as an integrated part of the California Current System and in their own right. Research along this line includes Bigelow and Leslie (1930), Skogsberg (1936), Shepard et al. (1939), Griggs (1974), Kelly (1985), Breaker and Mooers (1986), Strub et al. (1987), Chelton et al. (1988), Narimousa and Maxworthy (1989), Dewery et al. (1991), Brink and Cowles (1991), Breaker and Broenkow (1994), Rosenfeld et al. (1994), Ramp et al. (1997), Hickey (1998), Miller et al. (1999), Collins et al. (2000), and Lipphardt et al. (2006). During

Corresponding author address: X. San Liang, Harvard University, 29 Oxford St., Cambridge, MA 02138.
E-mail: liang@deas.harvard.edu

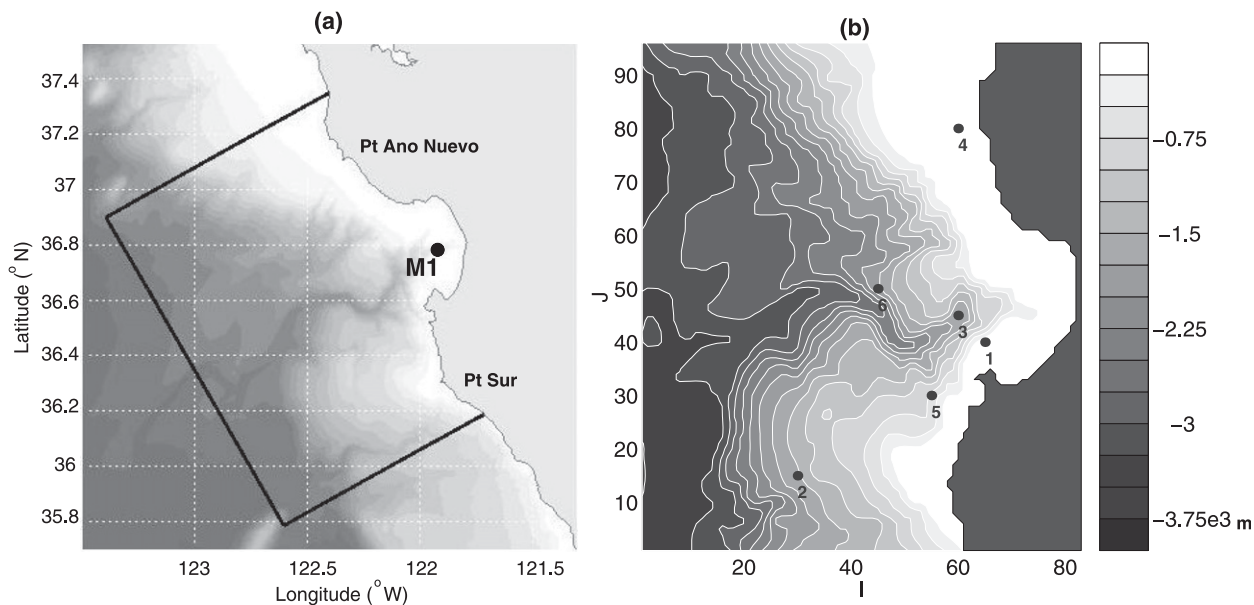


FIG. 1. (a) Research domain for the AOSN-II experiment. Marked are the two locations referred in the text: Point Año Nuevo and Point Sur, and the mooring station M1. (Courtesy of Patrick Haley, Jr.) (b) The enlarged and rotated (by 30° clockwise) domain overlapped with bottom topography (depth in meters). Also shown are the six locations where time series are extracted for spectral analysis. The coordinates are gridpoint indices.

August–September 2003, a multiinstitution, multiplatform comprehensive experiment of observations and forecasts, called Autonomous Ocean Sampling Network–II (AOSN-II), was conducted in this region. Densely covered data were collected and generated by a network of adaptive observational systems bringing together different sensors, robotic vehicles, and numerical ocean models. Many aspects of the experiment are discussed in a special issue of *Deep-Sea Research* (2008).

This paper studies the multiscale physical processes underlying the complex circulation during the AOSN-II experiment, and their relationship with the upwelling-related events. The multiscale complexity is one of the most prominent phenomena ever recognized in the Monterey Bay region. It is partly due to the varying external and internal forcings, partly due to the irregular domain geometry, and the nonlinear interplay between the two. Winds, buoyancy flows, local heating, eddies, mixing, oceanic fronts, and El Niño episodes, plus the curved coastline and the large submarine canyon, all need to be taken into account for a faithful reconstruction of the processes as observed (Rosenfeld et al. 1994). The problem is therefore rather generic; in other words, it would be very difficult to rely on simplification of certain factors to gain a convincing understanding of the dynamics. Clearly, the complex configuration and the highly variable environment pose a great challenge to our study.

During the past few years, a hierarchy of analysis methodologies and theories has been developed to ad-

dress this type of challenge (Liang and Anderson 2007; Liang and Robinson 2005, hereafter LR1; Liang and Robinson 2007, hereafter LR2; Liang 2008, manuscript submitted to *J. Fluid Mech.*). The philosophy behind these studies is that data-based geophysical fluid dynamics (GFD) theories may be developed independent of domain and other environment constraints, while numerical simulations can provide the data with arbitrary dynamic, geometric, and other configurations. These theories and methodologies are rigorous in mathematics and physics, without invoking any simplification or approximation, and have been applied with success to a variety of oceanic studies (e.g., Xie et al. 2007; P. Oddo 2007, unpublished manuscript; Liang and Robinson 2004, hereafter LR3) and engineering problems such as turbulence control (Liang and Wang 2004). Many problems, which otherwise would be very difficult, if not impossible, to investigate, turn out to be straightforward in their framework. In this study, we present an application of their multiscale energy and vorticity analysis (MS-EVA) and the MS-EVA-based theory of hydrodynamic stability, which are fully nonlinear and capable of handling oceanic and atmospheric processes intermittent in space and time.¹ Toward the end of this study, one will see that underlying a seemingly chaotic circulation, the dynamics are not that complicated. That

¹ A package of MS-EVA programs is available upon request.

is to say, underlying the complex Monterey Bay circulation, the source dynamical processes are tractable; the complexity arises from the interaction between two highly organized local instability modes established as the upwelling-favorable winds apply and relax.

The paper is organized as follows: we first give a brief introduction of the MS-EVA and the MS-EVA-based (fully nonlinear) localized instability analysis, followed by a short account of the dataset generated from the AOSN-II simulation. The analysis starts in section 4, where a large-scale window, a mesoscale window, and a submesoscale window are demarcated. The MS-EVA is set up in section 5. Processes are then projected onto the three scale windows, and the synthesized features are described in section 6. Sections 7 and 8 are devoted to a description of how kinetic energy (KE) and available potential energy (APE) are transferred from the large-scale background to mesoscale eddy structures. Particularly, section 7 gives a detailed analysis for the nonlinear baroclinic and barotropic instabilities associated with the variation of the prevailing winds. In section 9, the analysis is extended to the submesoscale window, and the multiscale dynamics inference is substantiated with some observations from the simulated fields. This study is summarized in section 10.

2. Perfect transfer (canonical transfer), localized hydrodynamic stability, and multiscale energy and vorticity analysis

The research methodologies for this study are the localized multiscale energy and vorticity analysis developed in LR1 and the MS-EVA-based theory of localized and finite-amplitude baroclinic instability and barotropic instability (LR2). The MS-EVA has been utilized to unravel the intricate dynamical processes underlying the meandering of the Iceland Faeroe Front (IFF), which is highly nonlinear and intermittent in space and time (LR3).

The MS-EVA is built on the basis of a new functional analysis machinery called multiscale window transform (MWT; Liang and Anderson 2007), which extends the traditional mean-eddy decomposition to retain local physics, particularly local energetics, and to allow for a faithful representation of the interactions beyond the mean and eddy processes (Liang and Anderson 2007). In this framework, a function space is decomposed into a direct sum of several mutually orthogonal subspaces, each with an exclusive range of time scales. Such a subspace is termed a *scale window*. The research task is, in an abstract way, to represent ocean processes on appropriate scale windows, and then to study how these processes evolve and interact in space–time through

exploring the window–window interactions. In the context of this study, we need a large-scale window, a mesoscale window, and a submesoscale window (denoted as $\varpi = 0, 1, 2$, respectively). Theoretically, demarcation of these windows does not require a basis, but for simplicity we appeal to orthonormal wavelet analysis to fulfill it, as in LR3. This yields three “window bounds”: j_0, j_1 , and j_2 , which are the wavelet scale levels marking the bounds of large-scale, mesoscale, and submesoscale windows, respectively. In other words, given a series with a time span τ , $2^{j_0}/\tau$, $2^{j_1}/\tau$ and $2^{j_2}/\tau$ are the higher-frequency bounds for the three windows.

On the three windows there exists a transform–reconstruction pair for the time-scale separation and multiscale energy representation. Suppose $\{\phi_n^j(t)\}_n$ is an orthonormal translational invariant scaling basis (built from cubic splines; see Liang and Anderson 2007), with j some wavelet scale level and n the time step. Let $S(t)$ be some square integrable function defined on $[0, 1]$ (if not, the domain can always be rescaled to $[0, 1]$). Before being analyzed, the domain needs to be extended to the whole real line. Different extension schemes will have different representations. We here just briefly show some results based on a periodic extension. In this case, there is a scaling transform

$$\hat{S}_n^j = \int_0^1 S(t) \phi_n^j(t) dt \quad (1)$$

for any scale level j (corresponding to frequency 2^j). Given window bounds j_0, j_1 , and j_2 , S then can be reconstructed on the three windows formed above:

$$S^{-0}(t) = \sum_{n=0}^{2^{j_0}-1} \hat{S}_n^{j_0} \phi_n^{j_0}(t), \quad (2)$$

$$S^{-1}(t) = \sum_{n=0}^{2^{j_1}-1} \hat{S}_n^{j_1} \phi_n^{j_1}(t) - S^{-0}(t), \quad (3)$$

$$S^{-2}(t) = S(t) - S^{-0}(t) - S^{-1}(t), \quad (4)$$

with the notations $\sim 0, \sim 1, \sim 2$ signifying the corresponding large-scale, mesoscale, and submesoscale windows. With these reconstructions, the multiscale window transform of S is defined as

$$\hat{S}_n^{\sim\varpi} = \int_0^1 S^{\sim\varpi}(t) \phi_n^{\sim\varpi}(t) dt, \quad (5)$$

for windows $\varpi = 0, 1, 2$, and $n = 0, 1, \dots, 2^{\sim\varpi} - 1$. In terms of $\hat{S}_n^{\sim\varpi}$, the above reconstructions on the three windows can be written in a unified way:

TABLE 1. Symbols for multiscale energetics (time step n , scale window ϖ). For details, refer to Liang and Robinson (2005).

Kinetic energy (KE)		Available potential energy (APE)	
\dot{K}_n^ϖ	Time rate of change of KE	\dot{A}_n^ϖ	Time rate of change of APE
$\Delta Q_{K_n^\varpi}$	KE advective working rate	$\Delta Q_{A_n^\varpi}$	APE advective working rate
$T_{K_n^\varpi}$	Total KE transfer	$T_{A_n^\varpi}$	Total APE transfer
$\Delta Q_{P_n^\varpi}$	Pressure working rate	b_n^ϖ	Rate of buoyancy conversion
$F_{K_n^\varpi, z}$	Rate of vertical dissipation	$F_{A_n^\varpi, z}$	Rate of vertical diffusion

$$S^{\sim\varpi}(t) = \sum_{n=0}^{2^{j_2-1}} \hat{S}_n^{\sim\varpi} \phi_n^{j_2}(t), \quad \varpi = 0, 1, 2. \quad (6)$$

Equations (5) and (6) form the transform-reconstruction pair for the MWT. Liang and Anderson (2007) showed that the energy for window ϖ local at time step n , E_n^ϖ , is simply $2^{j_2} (\hat{S}_n^{\sim\varpi})^2$ (up to some constant factor).

Within the MWT framework, the complex multiscale interactions can be conveniently represented. To illustrate, consider a field variable S advected by a flow \mathbf{y} ; S is a scalar field or the component of a vector. Coherent and smaller structures may be generated if both S and \mathbf{y} vary. Given the scale windows, the structure-generation problem is boiled down to finding how energy (quadratic quantities related to S) is transferred between them. Denoted by E_n^ϖ is the energy of S on scale window ϖ at time step n . It has been established that the transfer is

$$T_n^\varpi = E_n^\varpi \nabla \cdot \mathbf{v}_S, \quad \text{where } \mathbf{v}_S = \frac{(\widehat{\mathbf{v}S})_n^{\sim\varpi}}{\hat{S}_n^{\sim\varpi}}. \quad (7)$$

This theorem was briefly introduced in LR1 and later proved in Liang (2008, manuscript submitted to *J. Fluid Mech.*). In (7), \mathbf{v}_S has the dimension of velocity and has been referred to as S -coupled velocity. It may be viewed as a kind of averaged velocity with weights derived from the MWT of S . So with the MWT, the multiscale interaction in general, and the mean-eddy-turbulence interaction in particular, can be expressed succinctly as the divergence of the S -coupled velocity.

The above transfer T_n^ϖ is Eulerian and localized. It possesses a very interesting property, that is,

$$\sum_{\varpi} \sum_n T_n^\varpi = 0, \quad (8)$$

as proved in LR1. In other words, the transfer is a mere redistribution of energy among the scale windows. It does not generate, nor destroy energy as a whole. For this reason, it has been termed *perfect transfer* (or canonical transfer) in distinction to those transfers one might have encountered in the literature.

Following a similar procedure, the perfect transfers of KE and APE between scale windows can be derived. This allows for a precise separation of the intertwined nonlinear multiscale process in a system into a perfect transfer process and a transport process, and hence the establishment of a new energetic analysis methodology: MS-EVA. The MS-EVA diagnoses how energy is transported from one place to another or converted from one form to another (e.g., the conversion of mesoscale APE to mesoscale KE) within a scale window, and how energy is transferred between scale windows through hydrodynamic instability (e.g., the transfer of large-scale APE to mesoscale APE). Given a scale window ϖ ($\varpi = 0, 1, 2$) and a time step n , the time rate of change of kinetic energy (K_n^ϖ) and available potential energy (A_n^ϖ) are represented in the following equations (horizontal dissipation/diffusion ignored):

$$\dot{K}_n^\varpi = \Delta Q_{K_n^\varpi} + \Delta Q_{P_n^\varpi} + T_{K_n^\varpi} - b_n^\varpi + F_{K_n^\varpi, z}, \quad (9)$$

$$\dot{A}_n^\varpi = \Delta Q_{A_n^\varpi} + T_{A_n^\varpi} + b_n^\varpi + F_{A_n^\varpi, z}, \quad (10)$$

where the ΔQ terms represent the multiscale transport process on the specified scale window ϖ , and the T terms are the perfect transfers among different windows. Other notations are summarized in Table 1. Note that all the terms are localized in space and time; in fact, they are four-dimensional field variables, in contrast to the classical formalisms in which localization is lost in at least one dimension of space–time to achieve the scale decomposition. Processes intermittent in space and time are thus naturally embedded in (9) and (10).

The localized energetics in Eqs. (9) and (10) can be better understood with the aid of a schematic. Figure 2 presents the energy flow for the case of a two-window decomposition (window 0 and window 1), a simplified version of the three-window case (cf. Fig. 7 of LR1). From it one sees that buoyancy conversion always occurs within the same window (positive if from KE to APE), and the interplay between windows is through the T terms or perfect transfers. Note that there are no window indices assigned to T_K and T_A in the schematic, as they bridge two different scale windows. They should be understood as $T_{K_n^0}$ and $T_{A_n^0}$ if the large-scale energetics

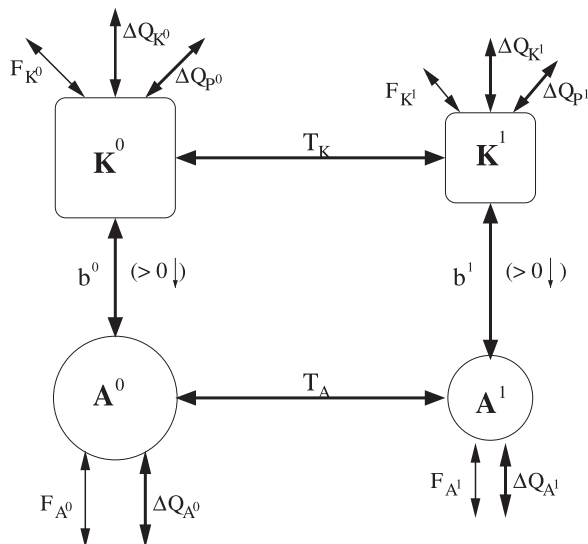


FIG. 2. A schematic of the energetics for a two-window decomposition. The symbols are the same as those in (9) and (10), except that the subscript n (time step) is omitted for simplicity. The windows 0 and 1 should be understood as, respectively, the large-scale window and mesoscale window (or “eddy” window). The buoyancy conversion is defined to be positive if it is from KE to APE. This schematic is a simplification of the three-window energy flowchart in the Fig. 7 of LR1.

are considered, while in the mesoscale energy balance they are $T_{K_n^1}$ and $T_{A_n^1}$, respectively.

The perfect KE and APE transfers $T_{K_n^0}$ and $T_{A_n^0}$ are very important in that they connect processes between different scale windows. It has been shown that these transfers are closely related to the classical GFD stability theory (LR2) and the classical hydrodynamic stability theory in the sense of Lyapunov (Liang 2008, manuscript submitted to *J. Fluid Mech.*). A localized hydrodynamic instability analysis was henceforth rigorously established, the results of which are presented here.

First consider a two-window system as schematized in Fig. 2. Its stability is quantitatively measured by the rate of energy transferred from the large-scale window to the mesoscale window. The T terms in Eqs. (9) and (10) should serve as the measure, but they involve transfers within their respective windows that are irrelevant to stability. That is to say, a T term contains not only the energy transfer across two different windows but also the energy exchange between different time steps within the same window. (This is an aspect that makes a localized transform different from the classical transforms. See LR1.) For the purpose of stability study, the latter must be excluded. This is done via an interaction analysis, on which we do not elaborate here. Details can be found in LR1 (section 9). We just use the superscript $\varpi_0 \rightarrow \varpi_1$ to signify such an analysis, selecting the com-

ponent from window ϖ_0 to window ϖ_1 ($\varpi_0, \varpi_1 = 0, 1$). With the interaction analysis, the total APE and KE transferred between the scale windows can be easily derived from the T terms. Particularly, $T_{A_n^0}^{1 \rightarrow 0}$ and $T_{K_n^0}^{1 \rightarrow 0}$ are the total APE and KE transfers from the mesoscale window (window 1) to the large-scale window (window 0). So,

$$BC = -T_{A_n^0}^{1 \rightarrow 0}, \quad (11)$$

$$BT = -T_{K_n^0}^{1 \rightarrow 0} \quad (12)$$

are the total APE and KE transferred from the large-scale window to the mesoscale window. The criteria of instability analysis based on (11) and (12) are, as those in LR2 and LR3,

- 1) a flow is locally unstable if $BT + BC > 0$, and vice versa;
- 2) for an unstable system, if $BT > 0$ and $BC \leq 0$, the instability is called barotropic;
- 3) for an unstable system, if $BC > 0$ and $BT \leq 0$, the instability is called baroclinic; and
- 4) if both BT and BC are positive, the system is undergoing a mixed instability.

For convenience, BT and BC may also be loosely referred to as barotropic transfer and baroclinic transfer, respectively.

The above instability analysis may be carried down to the transfers between the mesoscale and submesoscale windows. All the criteria are the same, except for a replacement of $1 \rightarrow 2$ for $0 \rightarrow 1$. In the three-window case, if the energy source is ultimately traced to the basic background, the nonlinear perfect transfer between the large-scale and mesoscale windows can be viewed as the representation of a primary instability, while that between the mesoscale and submesoscale windows represents a secondary instability. To avoid confusion, we only assign the shorthands BC and BT to the former. When a secondary instability is concerned, the full expressions $T_{A_n^1}^{1 \rightarrow 2}$ and $T_{K_n^1}^{1 \rightarrow 2}$ will be written out.

3. Hindcast fields of August 2003 with the Harvard Ocean Prediction System

In August–September 2003, a multi-institutional, multiplatform collaborative survey, including the deployment of two fleets of autonomous underwater vehicles (AUVs; more information is available online at <http://glider.who.edu/dmf> and <http://www-pord.ucsd.edu/~rdavis>) was conducted in the Monterey Bay region within a domain, as shown in Fig. 1a. This domain has

been referred to as the data domain (Haley et al. 2008). Nowcasts, forecasts, and hindcasts were launched based on the observations through nesting within an offshore domain (see Fig. 1 of Haley et al. 2008) 9 times larger toward a real-time estimation of the oceanic fields under best quality control. In this study, we consider a well-validated reanalysis output for the data domain from the Harvard Ocean Prediction System (HOPS). Presented here is a brief description of how the dataset was generated. For details, refer to Haley et al. (2008), Lermusiaux (2007), Li et al. (2008), Ramp et al. (2008), and the related HOPS product dissemination sites (more information is available online at <http://people.seas.harvard.edu/~leslie/AOSNII/REANALYSIS/index.html> and <http://people.seas.harvard.edu/~haley/work/HOPSreal-time.html>).

For the purpose of this study, only the data domain (Fig. 1b) is briefly described. It is horizontally discretized into a 83×96 mesh grid, with an equal grid spacing $\Delta x = \Delta y = 1.5$ km. In the vertical is a double-sigma coordinate frame, that is, a frame with two subframes of sigma coordinates, one above the other, for the two parts of a thermocline-separated vertical dimension. The nowcast/forecast starts on 2 August, using a time step size of 300 s. The whole process is data driven, using the densely covered data from the CTD surveys (Point Sur, R/V *John Martin*, and Point Lobos), the glider measurements [Woods Hole Oceanographic Institution (WHOI) and The Scripps Institution of Oceanography (SIO)], and the aircraft SST missions [Naval Postgraduate School (NPS)] throughout the experiment.

The model is initialized with the climatology. Observations are assimilated on a daily basis, allowing for the influences of the large-scale current systems, such as the California Current and California Undercurrent, to get in as the system is steered forward. The data assimilation is carried out using the optimal interpolation (OI) scheme associated with HOPS. On every simulation day at 1200 UTC, observed temperature and salinity are gathered within an interval of 36 h (18 h before and after that time) and objectively analyzed (OA), and error fields are accordingly obtained. Velocity is estimated from the analyzed temperature and salinity by geostrophic integration, assuming a level of no motion of 1250 m. Thirty-one assimilation fields are thus generated, spanning from 6 August to 5 September, plus five more for the initialization (2 August–5 August). For reference convenience, 6 August is labeled as day 1. Sequentially, 7 August through 7 September are called day 2, day 3, and so forth.

The horizontal open boundary conditions are obtained through a two-way nesting with the offshore domain (see

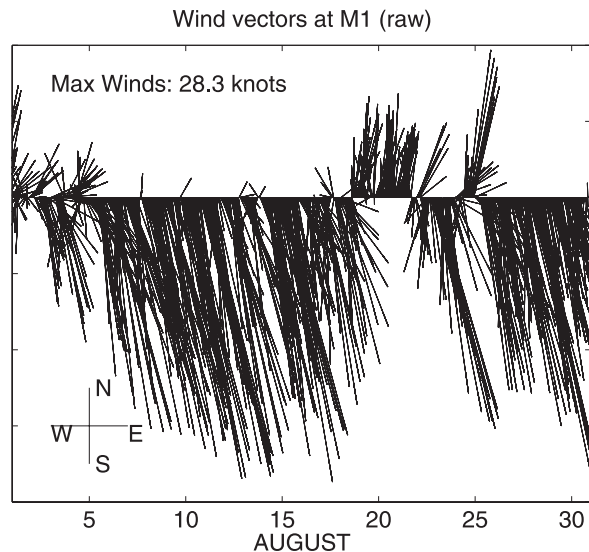


FIG. 3. Stickplot of the wind at M1 (36.755°N , 122.025°W) during the period of AOSN-II experiment.

Haley et al. 2008 for details). At the surface, atmospheric forcings, including fluxes of momentum, heat, and mass, are applied in a real-time mode. They are derived from the Coupled Ocean–Atmosphere Mesoscale Prediction System (COAMPS; from <ftp.nrlmry.navy.mil>) on a twice-daily basis, and then bicubically interpolated to the HOPS grids. Among these, the heat flux is a resultant net flux of shortwave radiation, longwave radiation, sensible heat flux, and latent heat flux; the net surface water flux out of the ocean is the difference between evaporation E and precipitation P .

Among the atmospheric forcings, winds play a dominant role in the upwelling process in this region (e.g., Rosenfeld et al. 1994). Shown in Fig. 3 are the stickplots of the wind at Mooring Station M1 (36.755°N , 122.025°W). During the experiment period, the maximal magnitude of the upwelling-favorable wind is attained on 11 August. It relaxes on 18–23 August. After that, another cycle starts and a second peak appears around 27 August.

This study focuses on the processes between these two wind stress peaks. The flow and tracer distributions are reconstructed and quantitatively and qualitatively validated. In terms of a variety of skill metrics, the simulation agrees well with the observation; particularly, it has captured the current reversals that occur when the wind ceases. For a detailed description of the reconstructed fields and their validation, refer to Haley et al. (2008). Briefly shown here are just two sequences of temperature and flow for depths 10 and 150 m (Fig. 4). These two depths are typical of the processes in the surface layer and the deep layer, respectively. From these plots it is easy to identify some

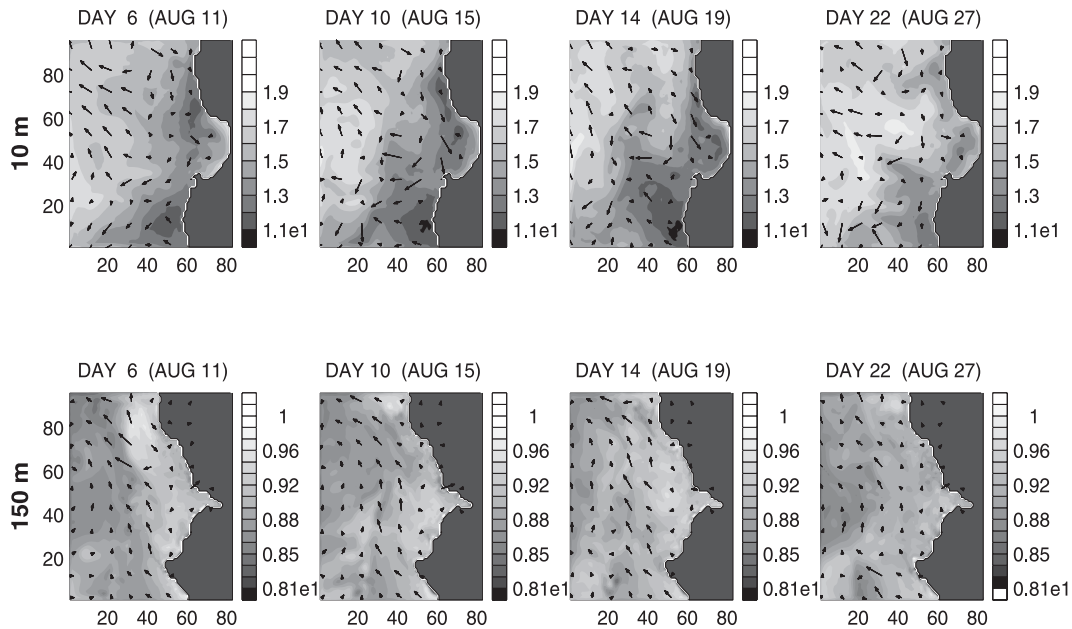


FIG. 4. Simulated temperature ($^{\circ}\text{C}$) for depths (top) 10 m and (bottom) 150 m.

features with dynamical significance. As is clear, the surface distribution is very complicated and much affected by the wind. There are two cold centers along the coast, one residing offshore Point Sur, another one between the Bay and offshore Point Año Nuevo. When the wind relaxes, warm water quickly takes over, in agreement with the previous observations (e.g., Rosenfeld et al. 1994). But the most intensive upwelling occurs outside Point Sur and the Bay mouth on 19 August, the day when the wind has just relaxed. Throughout the experiment, the net surface heat flux does not covary with the upwelling, and there is no shortwave radiation penetration through the water column (see Haley et al. 2008). In contrast to the surface layer, the deep layer is less affected by the winds and the processes seem to be simpler. Warm patches appear all the time outside Point Sur and within the Bay, and propagate northwestward along the coast, regardless of the winds.

4. Spectral analysis and window-bound determination

As in LR3, the window bounds needed for the MS-EVA analysis are determined through wavelet spectral analysis of point time series. The mooring M1 (36.755°N , 122.025°W ; cf. Fig. 1a) provides a set of such series. In case M1 does not capture the most important processes within the domain, we have also examined several time series extracted from the reanalysis data. Particularly, the time series from the following six

points (cf. Fig. 1) have been studied: point 1: (65, 40); point 2: (30, 15); point 3: (60, 45); point 4: (60, 80), point 5: (55, 30), point 6: (45, 50). These points are typical of the geography and flow pattern observed in the simulation. Specifically, points 1 and 3 are at the mouth of the Bay, and the latter is also over the canyon at the outer Bay; point 2 is in a very energetic region; points 4 and 5 are located offshore Point Año Nuevo and Point Sur, the two crucial places in dynamics, while point 6 is within a large surface anticyclonic eddy observed most of the time throughout the experiment. As the surface upwelling events are of special interest for this region, we focus on processes in the upper layers. To facilitate visual inspection, the means have been subtracted from all the time series before plotting the spectra.

Consider temperature first. In the spectrum of the M1 SST for the experimental period (not shown), a conspicuous feature is the peak between time-scale levels 2 and 4 (corresponding to 8 days and 2 days),² suggesting that a window demarcation with $j_0 = 2$ and $j_1 = 4$ will have the major temporal mesoscale processes

² The scales are $2^{-j} \times 32$ days ($j = 2, 4$), i.e., 8 days and 2 days. Note in connecting wavelet analysis to Fourier analysis, which is more familiar to the community, a common practice is to associate scale with frequency. This is a practical convenience, but is not entirely true. Given a time series, a scale in the wavelet sense actually contains a neighborhood of frequencies (see Strang and Nguyen, 1997). So the obtained scales of 8 days and 2 days should not be strictly identified with the periods of the processes.

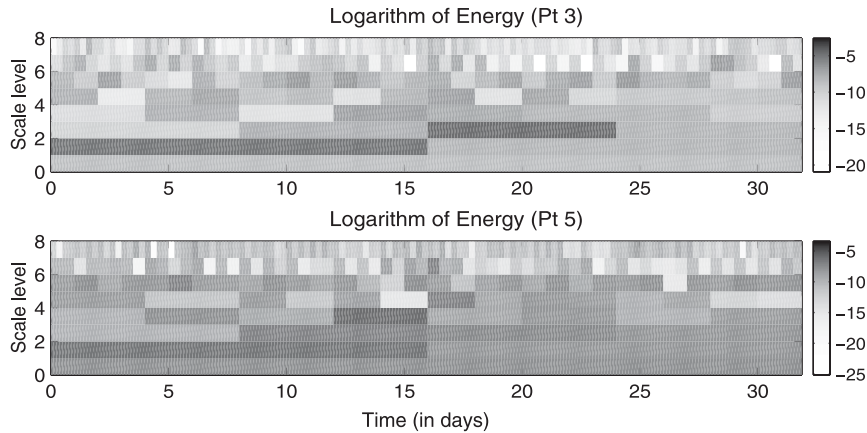


FIG. 5. Wavelet energy spectra for the surface temperature time series at (top) point 3 and (bottom) point 5. Shown here are the logarithms of wavelet energy, which is defined as the square of the wavelet transform coefficients divided by the corresponding time scale (Liu et al. 2007). The transform is with an orthonormalized cubic spline basis (cf. LR1 and LR3). The scale level j is defined such that 2^{-j} is equal to the time scale normalized by the duration (here 32 days). To facilitate visual inspection, the means have been subtracted from the series before the spectra are computed.

well represented. Of the six chosen points, points 3 and 5 are observed typical. Depicted in Fig. 5 are their respective temperature spectra. In both, there is a transfer of energy from low time-scale levels (long scales) to higher levels as time advances. The transfer starts on day 8, or 14 August, and is enhanced from days 12 through 16 (18–22 August), which is the wind relaxation period. At point 3, there is a strong transfer on day 16 to a temporal mesoscale event from both large scales and smaller scales, forming a very clear maximum at scale level 2 (8 days). All these events are related to the wind relaxation.

A similar trend is also seen on the velocity spectra. Points 4 and 5 are found to be two typical points. (Point 3 is similar to point 4, but with features not as enhanced as that of point 4.) Shown in Fig. 6 are the spectra for v at (top) point 4 and u at (bottom) point 5. Spectra for the other components are not shown, because u is much weaker than v at point 4 and the spectrum for v is similar to that of u at point 5. Again, the energy transfer is clearly seen, but the timing differs. At point 4, it begins on day 8 (14 August), is enhanced on day 16, and lasts through day 24 (30 August). The peak takes place at time-scale level 2, corresponding to a period of 8 days. At point 5, the transfer period is from day 12 (18 August) through day 20 (6 August), and the maximum is at time scale level 3 (4 days).

According to the above analysis, if one focuses on the relaxation events, both the temperature and velocity spectra support a time-window partitioning with

$j_0 = 2$ (8 days) and $j_1 = 5$ (1 day). That is to say, processes with time scales longer than 8 days should be included in the large-scale window, while those shorter than or equal to 1 day are left for the submesoscale window. A sensitivity study was performed, showing that the resulting MS-EVA analysis is robust around this set of parameters. We have tested $(j_0, j_1) = (2 \pm 1, 5)$, $(2, 5 \pm 1)$; the results are all similar to that with $(2, 5)$.

The MS-EVA terms in (9) and (10) need to be horizontally treated to remove the small-spatial-scale phase oscillation that may arise from the multiscale window transform (LR1, section 7). The treatment is equivalent to a horizontal low-pass filter (formed with orthonormalized cubic splines; see Strang and Nguyen 1996). In this study, the phase oscillation is found not to be a problem, in contrast to that in LR3. We simply choose to remove the features with horizontal scales smaller than 4 grid sizes, or 6 km. Experiments have been performed with a horizontal filter scale of 6 and 8 grid sizes, and the results are the same.

5. MS-EVA setup

In the present version, the MS-EVA uses flat coordinates in the vertical dimension. The double-sigma coordinates of the HOPS hindcast need to be interpolated onto flat z levels. The chosen levels are summarized in Table 2. We select depths 0, 10, 30, 150, and 500 m for our analysis. Among them, depth 10 m is within the mixed layer (either the top, middle, or bottom, depending on the winds), depth 30 m lies in the middle of

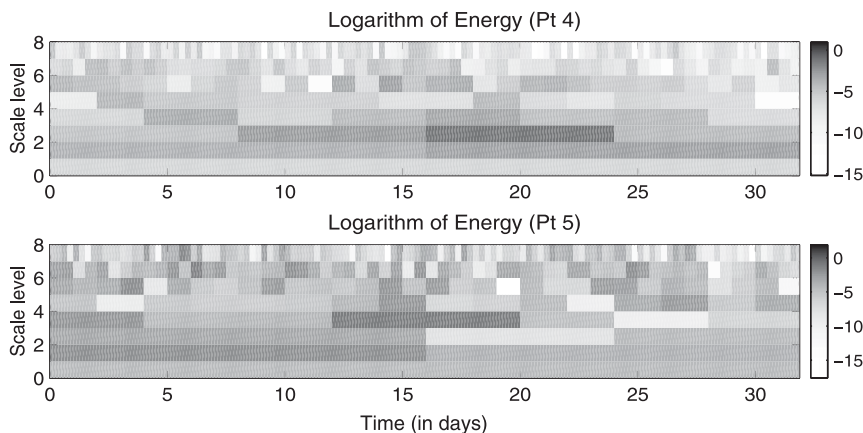


FIG. 6. Spectra for the surface velocity (top) component v at point 4 and (bottom) component u at point 5.

the thermocline, depth 150 m is roughly at the bottom of thermocline and in the core of the California Undercurrent, while depth 500 m cuts across the deep California Current System (see Haley et al. 2008). The necessary fields are linearly interpolated onto these levels.

A mean profile of $\bar{\rho} = \bar{\rho}(z)$ is needed for the available potential energy analysis. The mean is computed by taking an average of ρ over all the available data points and time instants from the simulation. Table 2 gives a brief summary of the needed parameters.

6. MS-EVA analysis: Description of fields

With the parameters in Table 2, it is straightforward to reconstruct features on the prescribed scale windows. This section gives a description of these multiscale features. The governing dynamics will be presented in the next section.

a. Temperature

Understanding the temperature distribution and its variation in response to the upwelling-favorable wind is a major goal for the Monterey Bay circulation study. The response is reflected on different time-scale windows. Figure 7 presents a sequence of the large-scale reconstructions of temperature for vertical levels 2 (10 m) and 12 (150 m). In the upper layer, a belt of cold water dominates along the coastline. The upwelled water is organized into two cold centers: one within the Bay, another outside Point Sur. This horizontal structure is most conspicuous around 15 August and becomes weakened through the end of the month. In contrast, the interior region is characterized by a large pool of warm water. As time goes on, the pool gets enlarged and eventually takes over the whole western part of the domain at depth 10 m.

There is a distinct vertical structure on the large-scale temperature field. In deep layers, the water is generally warmer along the coastline and cooler seaward, as shown in Fig. 7c. The trend reversal of offshore temperature gradient occurs roughly at 100 m (not shown).

The temporal mesoscale temperature is rich in structure and process. This is particularly so in the surface layers. Shown in Fig. 8 is the mesoscale temperature evolution at level 2 (10 m). Three major events are clearly seen during the period day 6 (11 August) through day 22 (27 August). On day 6, a dipole shows outside the Bay, with warm water in the south. There is no evidence that this dipole propagates. Rather, it grows and oscillates in time, with shape changing accordingly. On day 14 (19 August) it reaches its minimum in low temperature, and on day 18 (23 August) the phase is reversed. As a result, a large pool of cold water appears in the middle of the domain on 19 August. Comparing to Figs. 4, 7, the sudden cooling of water on this day should be a secondary upwelling. We shall come back to this issue later on in the MS-EVA analysis.

A new structure begins to emerge north of the Bay outside Point Año Nuevo on day 12, which becomes

TABLE 2. Parameters for the application of MS-EVA.

Parameters	Value
Time window bounds: j_0, j_1	2, 5 (8 days, 1 day)
Spatial filter	6 km (4 grid points)
$\bar{\rho}(z)$	See the text
Grid	$83 \times 96 \times 22$
Time stepsize Δt	3 h
Horizontal grid spacing $\Delta x, \Delta y$	1.5 km
Vertical level depths (levels 1–22, in meters):	
	2.5, 10, 20, 30, 40, 50, 60,
	72.5, 90, 110, 130, 150, 170, 202.5,
	250, 300, 350, 400, 450, 500, 550, 600

LARGE-SCALE TEMPERATURE

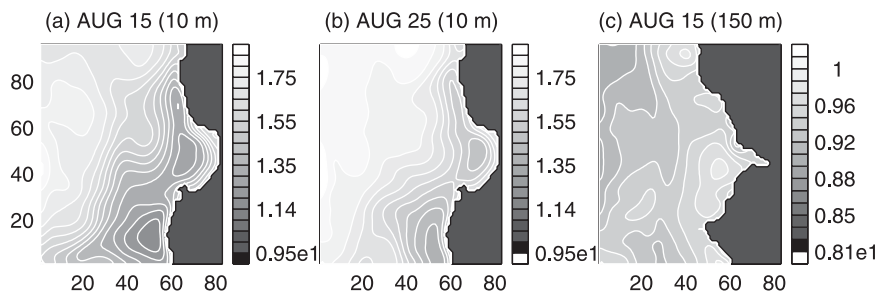


FIG. 7. Large-scale temperature ($^{\circ}\text{C}$) for depths 10 and 150 m.

evident by day 14 (19 August), and strong enough on day 16 (21 August) that it then seems to propagate northward along the coast. The third event is found on 13 August as a dipole near the southwestern corner, with a cold center to the west. This dipole keeps growing until the wind relaxes, when it begins to move northward on 21 August. Extended simulations for one more month indicate that there could be a northward propa-

gation, with an estimated speed of 0.08 m s^{-1} (not shown). We have computed coastal trapped wave (CTW) properties with the averaged buoyancy frequency profile and topography for this region (see appendix A); we find that one thermocline-trapped CTW mode has a phase speed of 0.09 m s^{-1} .

The processes in deep layers are relatively simple. At level 12 (150 m), cool and warm pools emerge within the

MESO-SCALE TEMPERATURE (10 m)

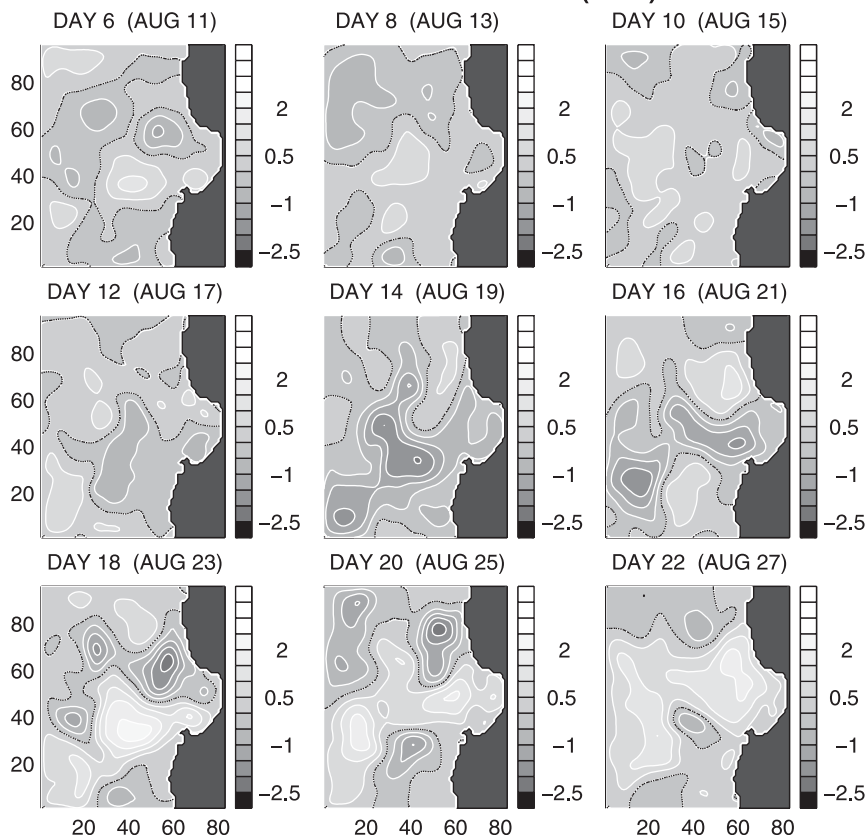


FIG. 8. Sequence of mesoscale temperature ($^{\circ}\text{C}$) at depth 10 m. The black dotted line marks the zero contour.

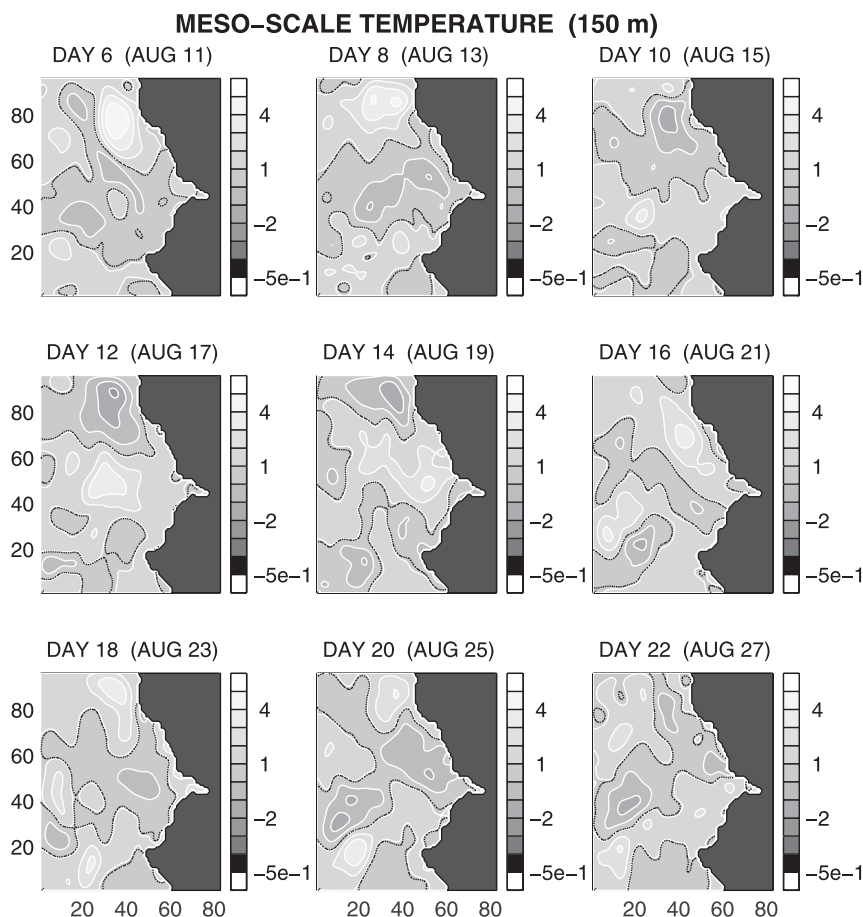


FIG. 9. Sequence of mesoscale temperature ($^{\circ}\text{C}$) at depth 150 m. The black dotted line marks the zero contour.

Bay and move northward along the coast (Fig. 9). From the results of the extended simulations (not shown), this also seems to be some CTW propagation.

b. Velocity

The flow field is also rich in scale. Figure 10 shows the large-time-scale reconstructions for levels 2 (10 m) and 12 (150 m). They are typical of the flows for the surface layers and deep layers. By comparison, the flow at level 2 is more complex. Roughly, it can be classified into two types: one coastal current flowing southward, one northward current offshore pertaining to the California Countercurrent (CCC). But this trend is interrupted by a cyclonic gyre outside Point Sur. For the deep layers, the flow pattern is much simpler. The whole system is characterized by a strong northward along-slope current, with a weaker California Undercurrent to the west. The general trend of the large-scale current weakens toward the end of August.

On the mesoscale window, the flow exhibits itself in a complicated pattern in upper layers, particularly

in surface layers (Fig. 11). In the 10-m sequence, the strength of variability does not change much until the wind relaxes (cf. the distribution of 17 August, or day 12, in the figure), when a burst of variability appears that lasts toward the end of the month. Eddy structures are generated, advected, and diminished here and there, making the flow a very complex system. We will return to the analysis later with more powerful methodologies.

The deep-layer variability is relatively simple. Drawn in Fig. 12 is a sequence of the 150-m mesoscale flow. Generally, the variability is in the form of a dipole outside the northern part of the Bay. The variability keeps being generated near the Bay area during 11 through 23 August (days 6–18). It then moves northward, weakens, and finally disappears just near the northern boundary. In some sense, it may be summarized as a source outside the Bay, plus a sink near the northern boundary.

c. Multiscale energy

Multiscale energy distributions reveal more information about the ocean response to the external forcing.

LARGE-SCALE FLOW

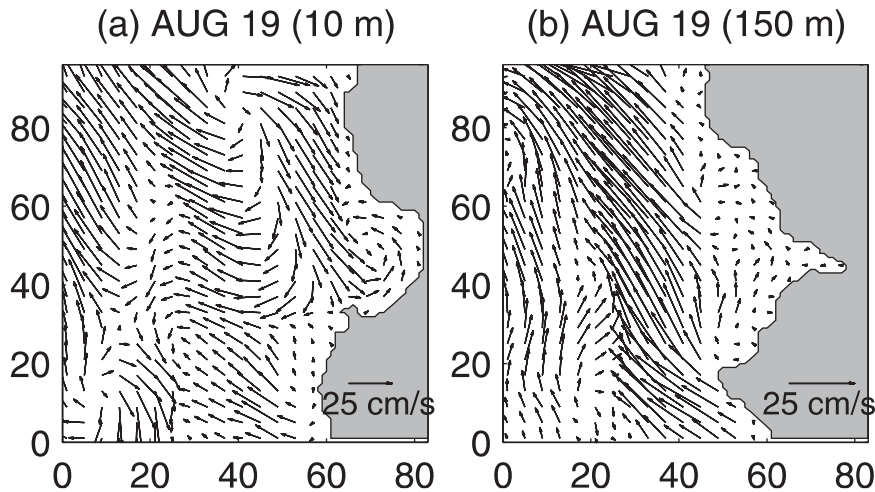


FIG. 10. Large-scale velocity for (a) depth 10 m and (b) depth 150 m.

As will be seen later, the effect of winds enters the energy balance mainly through the large-scale window. For this reason, we first look at the large-scale energy and its variation.

At depth 10 m, the large-scale potential energy (Fig. 13, top) exhibits its features in two regions: one lies mainly in the Bay, another off Point Sur. In both regions, APE grows as time advances from 11 to 15 August, then goes down toward the end of the month. Sometimes the hotspot within the Bay extends northward to Point Año Nuevo.

A similar structure also exists on the surface-layer large-scale KE sequential maps (Fig. 13, bottom), and their variations also follow a similar trend. The difference is that the southern counterpart lies far offshore, and it becomes strengthened again after the relaxation period (18–23 August). Another difference is that there is a third hotspot located in the northwest. It is strongest on 11 August during the period of concern. The next section shows how the dynamics underlying this KE hotspot are completely different from the other two.

The deep-layer large-scale energy reveals a different pattern of distribution. Drawn in Fig. 14 is the large-scale APE and KE of 15 August for depth 150 m. Obviously, the flow stores its APE (left) on the coastal side and in the northwestern corner, while kinetically it is most energetic along the shelf break. The largest kinetic energy occurs on 11 August. It decreases afterward through the survey period (not shown).

d. Bay mode and Point Sur mode

Identified in the above are two large-scale energy centers in the surface layer, which vary in some related

pattern as the wind applies (Fig. 13). A significant part of the kinetic energy, and almost all the potential energy, is organized into such a structure. One may use the term *mode* to describe this structure. But it is not a mode by traditional definition, as the two centers do not covary in response to the applied forcing. Nonetheless, one might as well regard the two centers as two distinct modes, that is, two localized modes in the framework of the localized analysis. They will be henceforth referred to as the Bay mode and the Point Sur mode, respectively. Notice that the Point Sur mode does not coincide in location on the APE map and the KE map. In the next section one will see that this mode is more consistent with respect to the internal driving forces, namely, the perfect transfers.

7. MS-EVA analysis: Barotropic and baroclinic transfers

The multiscale processes are governed by multiscale dynamics. In this section, we focus on the interaction between large-scale and mesoscale windows, which is measured by two field metrics, the barotropic transfer and baroclinic transfer. These metrics have been connected to barotropic instability and baroclinic instability in a generalized sense (cf. section 2).

a. Surface layers

As is shown in the preceding section, the dynamics of the upper layer is relatively complex. We calculate its BT and BC distributions to distinguish intrinsic mechanisms from extrinsic mechanisms. Again, level 2 (10 m) is found typical of the upper layer in this regard.

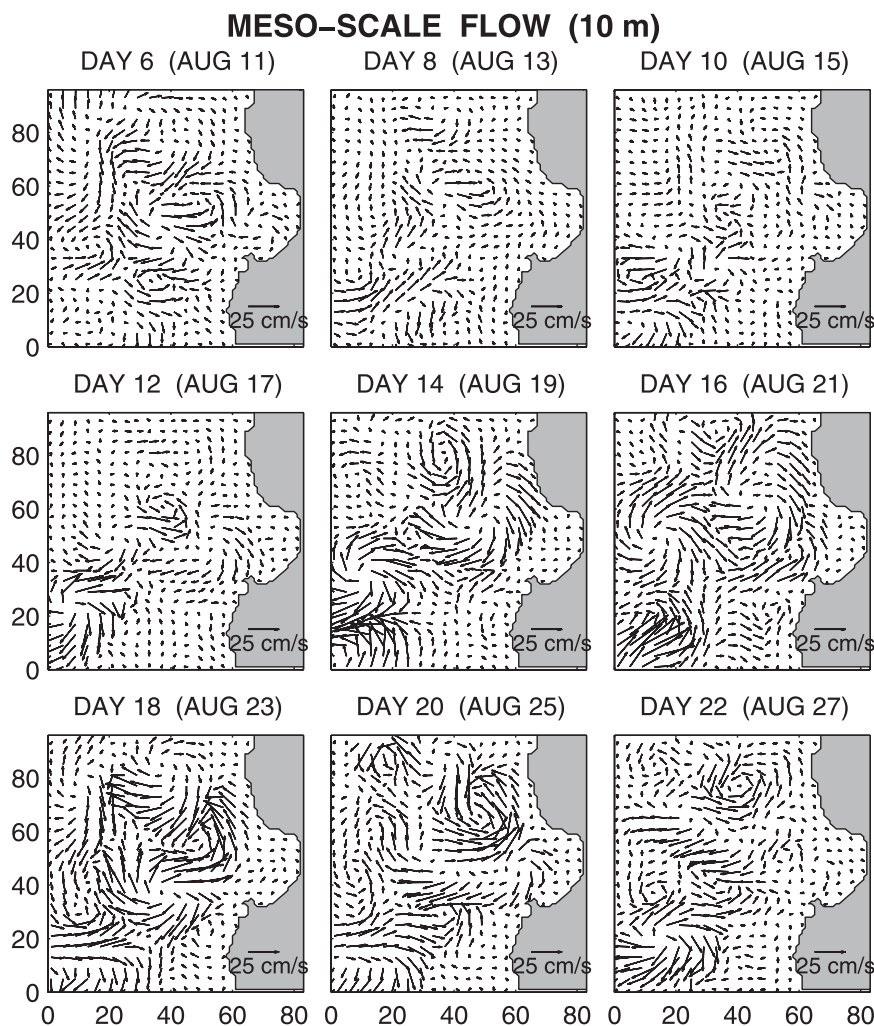


FIG. 11. Sequence of mesoscale velocity at depth 10 m.

Figures 15 and 16 depict how BC and BT evolve with time on this level.

Look at BC first. A remarkable feature is its bimodal structure: clearly shown in the sequence of Fig. 15 are two positive BC centers. We look at the southern one first. Starting from 11 August, it emerges in the domain outside Point Sur. It becomes stronger as time goes on and reaches its maximum on 15 August. After that, the transfer strength decreases until 19 August when it splits into two parts. The northern part eventually merges into another center farther north, which we will describe soon. The southern part reappears after 23 August. This BC hotspot corresponds well in variability to the Point Sur mode on the large-scale APE maps (Fig. 13), except that the Point Sur mode of APE sticks tightly to the coastline. Recall that positive BC means loss of energy to the mesoscale window. So the correspondence between BC and the large-scale APE indicates that the

wind stores energy in the large-scale window, and then releases it to mesoscale processes. On the other hand, the discrepancy in location between them implies that the energy could first build up near Point Sur, then be transported westward and released. This scenario will be clear in section 8a.

Another positive center on the sequential maps is located between the Bay and Point Año Nuevo. In comparison to the Bay mode on the maps of Fig. 13, the location is slightly northward. But for convenience we will still refer to it as the Bay mode—it gives rise to the Bay mode of APE, as will be seen in section 8a. This mode does not emerge until 15 August 15, when the wind decreases. It reaches its maximum on 21 August and weakens afterward.

Both the two BC hotspots covary with the wind during the major time of the event. The Point Sur mode generally follows the wind variation, with a phase lag of

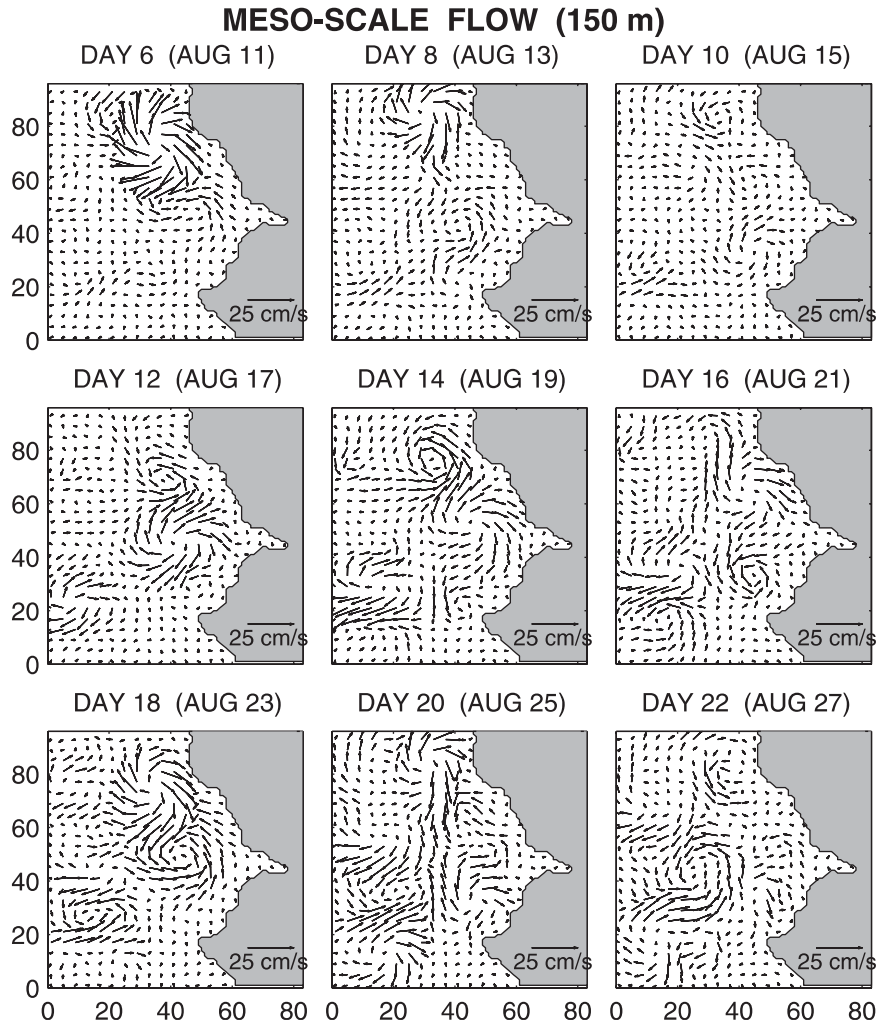


FIG. 12. Sequence of mesoscale velocity at depth 150 m.

2–3 days. In contrast, the Bay mode coincides negatively with the wind. The different coincidences indicate that the two baroclinic instabilities are triggered through different mechanisms, as shown below.

The opposite coincidences with the wind and hence the relative variation between the two modes suggest some kind of relation between the two transfer centers. It is not clear whether this means a conservation law while the two modes interact. But one does observe interactions between them, and, particularly, interactions are observed during the relaxation period. They are marked by the splitting of the Point Sur mode, which should exchange energy and information as well.

On the BT maps (Fig. 16), there is also a bimodal structure, and a similar evolution pattern is observed. The difference between BT and BC is that the two modes of BT are located a little southward and eastward before the wind relaxes and that the Point Sur center

becomes negative during the relaxation period. In this case, the Bay mode is really within the Bay before 17 August, but the Point Sur mode is far from the coast. The coincidences of the two centers with the wind are also opposite, just as that on the BC maps.

Although BC and BT follow a similar variability pattern with the wind, the wind influence seems to be more conspicuous on the BT evolution. In the south, negative transfer appears in the vicinity of the southwestern corner during 18–23 August; in the middle, the hotspot jumps from within the Bay on 17 August to where the BC Bay mode resides. Both these prominent variabilities occur in response to the wind relaxation, indicating a closer relationship of BT to external forcing.

The BC and BT distributions show that the system is unstable in the upper layer within the Bay after 11 August, because $BC + BT$ is positive (cf. Fig. 17), and the instability is of a mixed type. The most unstable case

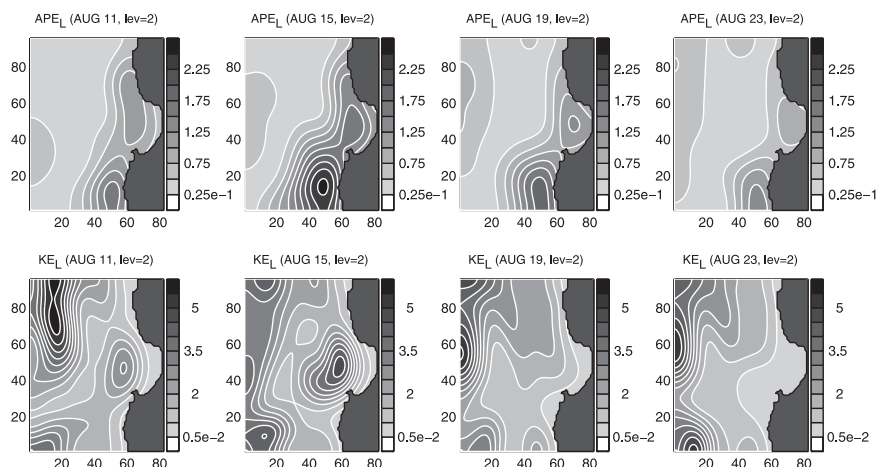


FIG. 13. A time sequence of large-scale (top) available potential energy ($\text{m}^2 \text{s}^{-3}$) and (bottom) kinetic energy ($\text{m}^2 \text{s}^{-3}$) for level 2 (10 m). (Note different scales for the shadebars.)

occurs during the relaxation period, 18–23 August. Off Point Sur, the flow is also unstable, except for the relaxation period, and the instability is also of a mixed type. But it is dominated by baroclinic instability before 18 August and switched to barotropic instability after 23 August. During the relaxation period, the flow tends to be stabilized outside Point Sur. The coincidences of BT and BC with the wind indicate that these instabilities are, to an extent, triggered externally.

b. Deep layers

The deep-layer transfer patterns are much simpler than their surface counterparts. Shown in Fig. 18 are the (left) BC and (right) BT on 15 August for the depth 150 m. On the BC map, the whole domain is characterized by a positive center within the Bay, and a weak negative center to the west of Point Sur. All the other regions are

virtually zero in transfer. This simple distribution keeps its structure through the entire experimental period, though the hotspot weakens, and the negative center disappears during the relaxation (not shown).

The 150-m BT and its evolution are also simpler than the surface BT. In Fig. 18 (right), it is basically composed of three distinct centers: a positive hotspot in the middle, a negative center to the north, and another weaker positive center to its south. The southern center varies in a way similar to the Point Sur mode at depth 10 m as shown in Fig. 16, and also becomes negative when the wind relaxes. The northern center is always negative, forming a sink to certain perturbations. This is consistent with what one has observed in the mesoscale flow plots (Fig. 12).

Worth special attention is the middle hotspot. It exists from 12 to 23 August and does not vary much during the

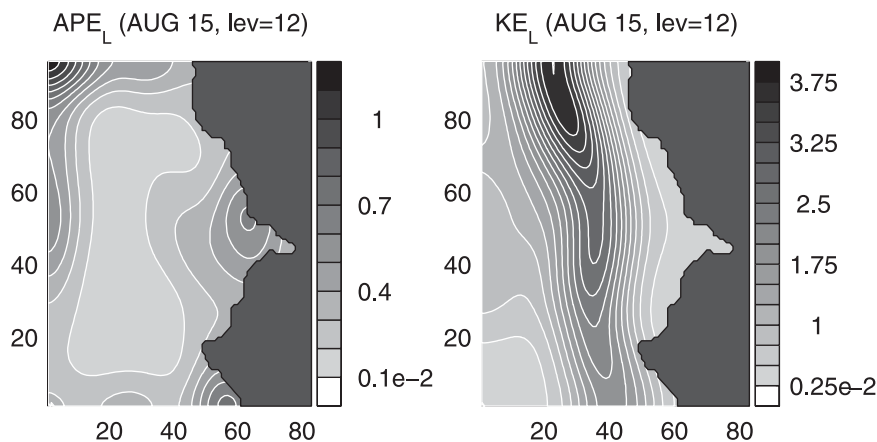


FIG. 14. Large-scale (left) available potential energy ($\text{m}^2 \text{s}^{-3}$) and (right) kinetic energy ($\text{m}^2 \text{s}^{-3}$) at level 12 (150 m) for 15 Aug 2003.

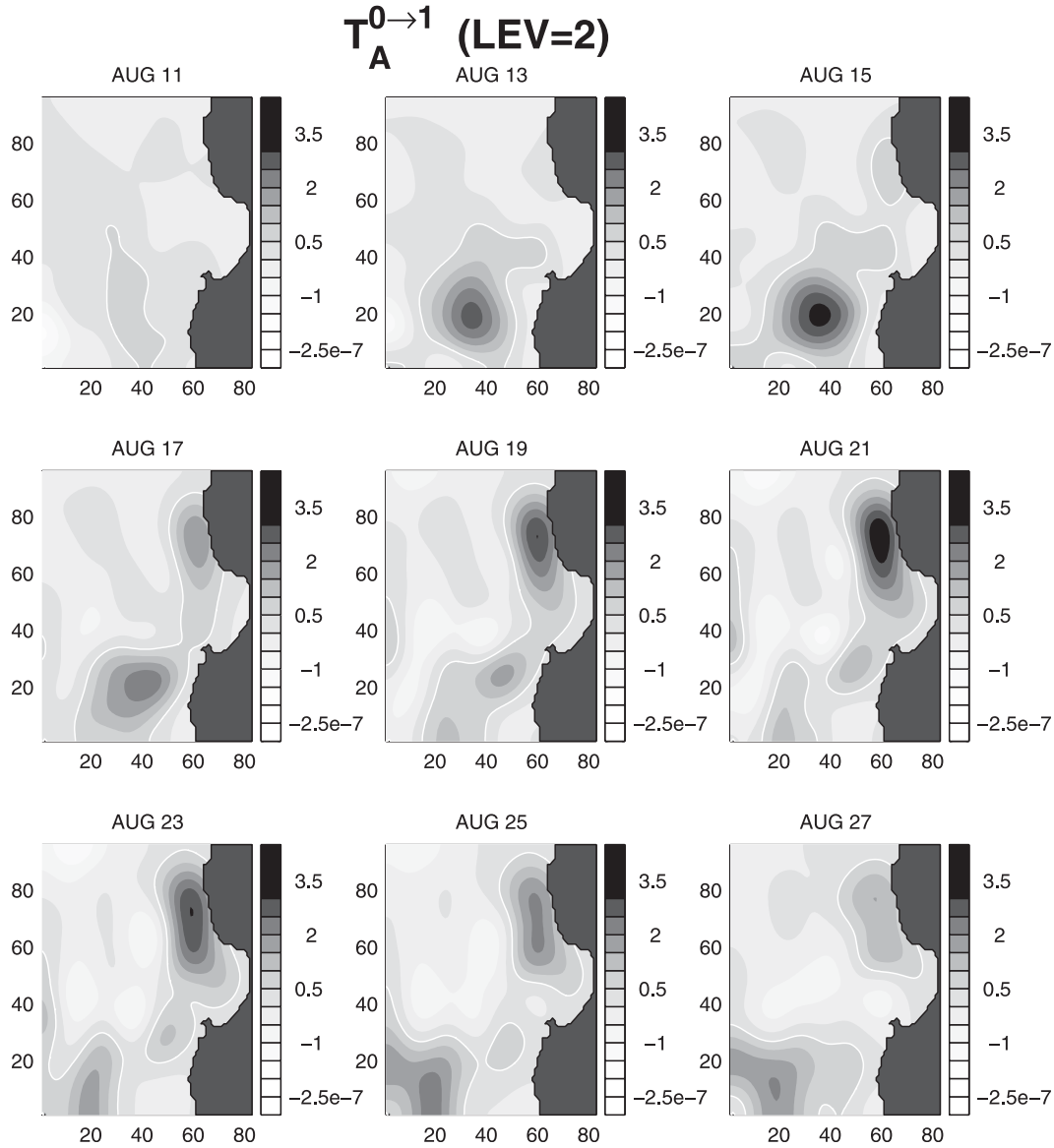


FIG. 15. Potential energy transfer ($m^2 s^{-3}$) at depth 10 m from large-scale window to mesoscale window (BC). The white solid line marks the zero contour.

period, neither in strength nor location. Clearly it has nothing to do with the wind. Compared to the topography in Fig. 1 and the flow in Fig. 10, it sits just downstream of the deep canyon. It might be caused by the California Undercurrent flowing over the canyon, a mechanism distinctly different from that of other positive centers.

8. MS-EVA analysis: Energy balance

We have examined the baroclinic and barotropic transfers during the large-mesoscale interactions and explored the relation between these transfers and the wind. This

section investigates the other MS-EVA terms in the energy balance. Because it is observed that the external forcing enters the equation mainly through the large-scale window, only the large-scale MS-EVA is considered.

a. Point series

We first choose two locations, S: (30, 15) and B: (57, 55), to study the problem (see Fig. 17). These locations are associated with the two distinct transfer centers over the experimental period. For convenience, we refer to them as S (Sur) and B (Bay), respectively. Plotted in Fig. 19 is the time series of the large-scale MS-EVA terms at point S. One observation is that external

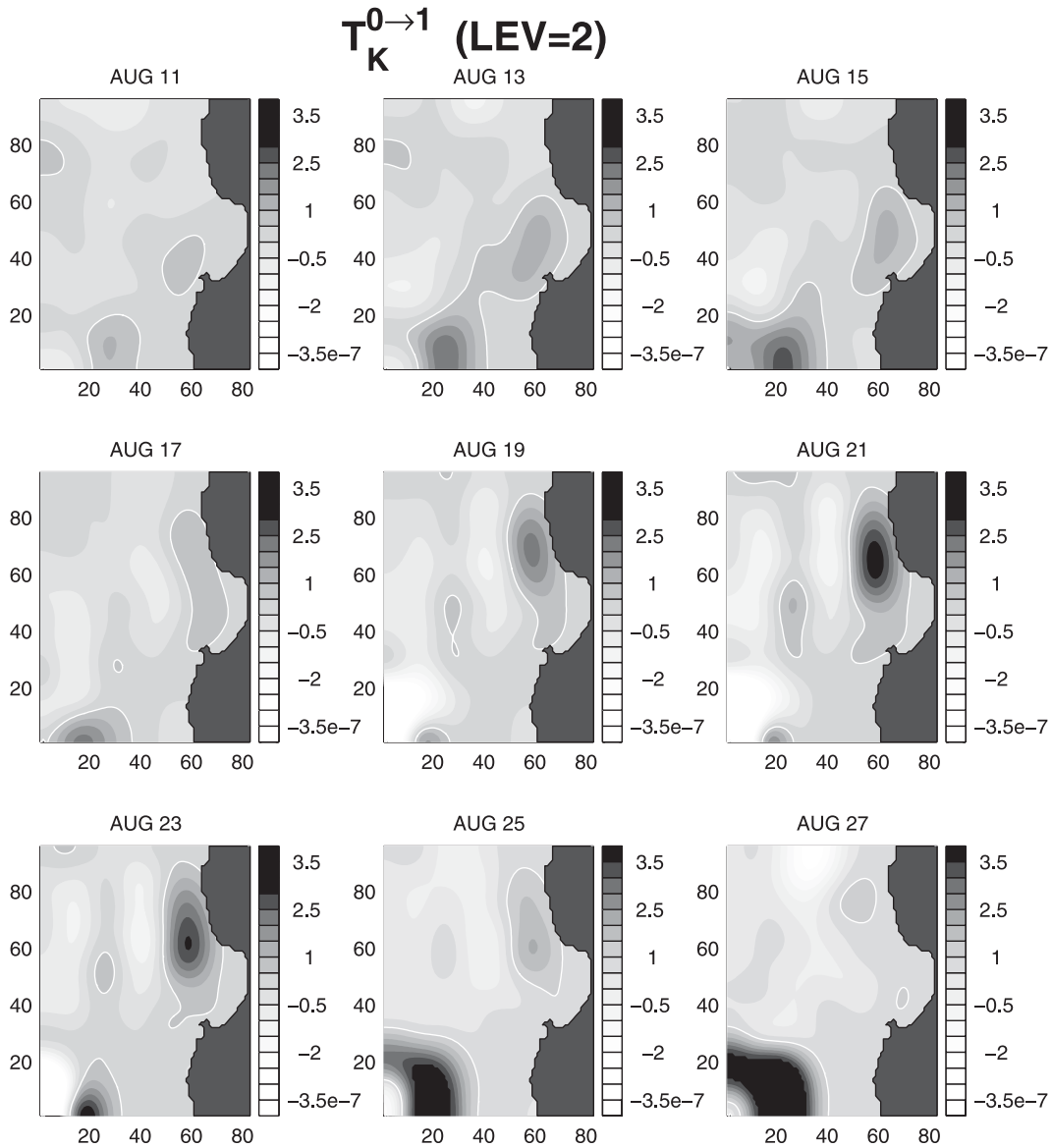


FIG. 16. Kinetic energy transfer ($\text{m}^2 \text{s}^{-3}$) at depth 10 m from large-scale window to mesoscale window (BT). The white solid line marks the zero contour. For comparison purpose, contours with values exceeding $\pm 3.5 \times 10^{-7} \text{m}^2 \text{s}^{-3}$ are not drawn.

forcing contribution ($F_{A_n^0, z}$) dominates the balance. Another observation is that buoyancy conversion (b_n^0) is rather weak. Balancing the work due to the external forcing is mainly from the horizontal advection in the APE equation ($\Delta Q_{A_n^0, h}$), and the horizontal pressure work in the KE equation ($\Delta Q_{P_n^0, h}$). The importance of other terms varies with time and location, but in the APE plot external forcing ($F_{A_n^0, z}$), advection ($\Delta Q_{A_n^0, h}$), and baroclinic transfer ($T_{A_n^0}$) dominate the balance throughout the duration of the experiment.

The simple balance between $\Delta Q_{A_n^0, h}$, $F_{A_n^0, z}$ and $T_{A_n^0}$ offers an explanation about the discrepancy observed

between the locations of BC and APE for the Point Sur mode (cf. the 15 August map in Figs. 13, 15). The positive coincidence between $F_{A_n^0, z}$ and $T_{A_n^0}$ and the negative coincidence between $\Delta Q_{A_n^0, h}$ and $T_{A_n^0}$ indicate that the energy transferred to the mesoscale eddies is not from the in situ large-scale energy instilled by the external forcing but from its neighborhood via advection. Clearly, large-scale energy first builds up near Point Sur. It is transported westward some distance and is then transferred to the mesoscale window through an instability, leading to the generation of mesoscale eddies.

$$T_K^{0 \rightarrow 1} + T_A^{0 \rightarrow 1} \quad (\text{LEV}=2)$$

AUG 15

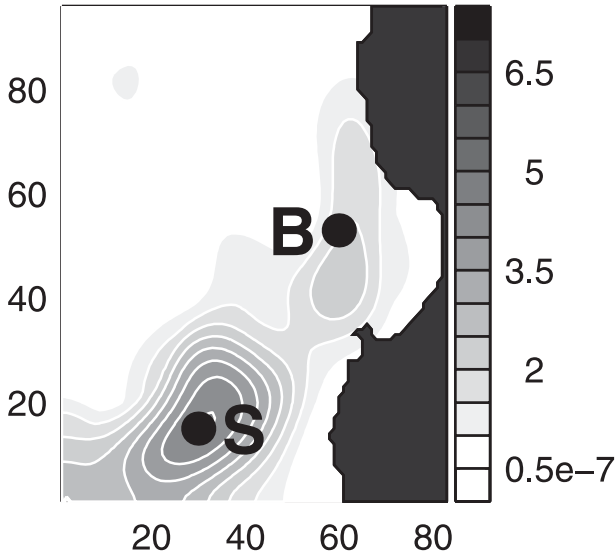


FIG. 17. BC + BT ($\text{m}^2 \text{s}^{-3}$) at depth 10 m for 15 August. The two points, B(57, 55) and S(30, 15), are marked for use in section 8.

Both the baroclinic transfer and the barotropic transfer make significant contributions to their respective equations. As noted before, BC and BT are equal to $-T_{A_n}^0$ and $-T_{K_n}^0$ followed by an interaction analysis that selects the part from large-scale window to the meso-scale window (indicated as superscript $0 \rightarrow 1$ in the

text). The variations of $T_{A_n}^0$ and $T_{K_n}^0$ then reflect the BC and BT, except for a negative sign. Because energy does not convert much between the two types, these transfers are the main indices for the temperature fluctuation and flow variability, respectively. In this sense, although the instability has an ingredient of baroclinicity, it is not eddy-like, as the buoyancy conversion is rather weak.

The coincidence between the external forcing and the transfers is clearly seen from the plots. In Fig. 19a, the transfer strength corresponds well with $F_{A_n}^0$. Particularly, $-T_{A_n}^0$ reaches its maximum just a couple of days after the $F_{A_n}^0$. (Recall that negative $T_{A_n}^0$ is related to instability.) The same observation is made in Fig. 19b before 23 August, when the wind relaxes. The largest negative value of $T_{K_n}^0$ occurs on 13 August, while on the same day the wind instills the largest part of energy. When the wind relaxes, the transfer becomes positive, that is, the flow is stabilized, in agreement with the previous observation with the BT sequence. After 23 August, this region experiences another instability, but the driving mechanism seems to be changed. Nonetheless, one can safely say that the Point Sur instability mode is directly driven by the external forcing.

For point B, which is associated with the Bay mode, the energetic scenario is similar with the APE equation (Fig. 20). The most significant balance is still between the external forcing, the horizontal advection, and the baroclinic transfer, and the variation trends of the three also have a resemblance to Fig. 19. Following the same argument as that of point S, one may explain away the location discrepancy between the BC center and the APE center of the Bay mode (cf. Figs. 15, 13): the Monterey Bay provides the necessary energy for the BC

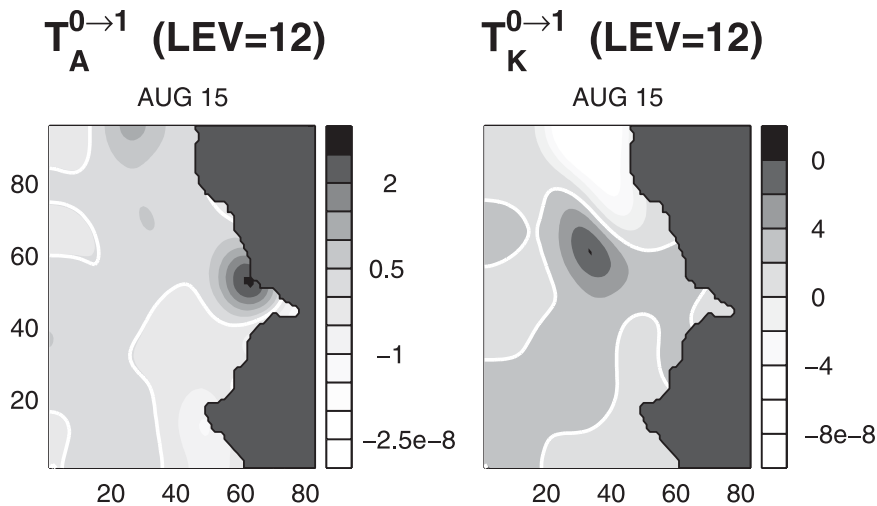


FIG. 18. (left) Potential energy transfer ($\text{m}^2 \text{s}^{-3}$) and (right) kinetic energy transfer ($\text{m}^2 \text{s}^{-3}$) at level 12 (150 m) from large-scale window to mesoscale window. The white solid line marks the zero contour.

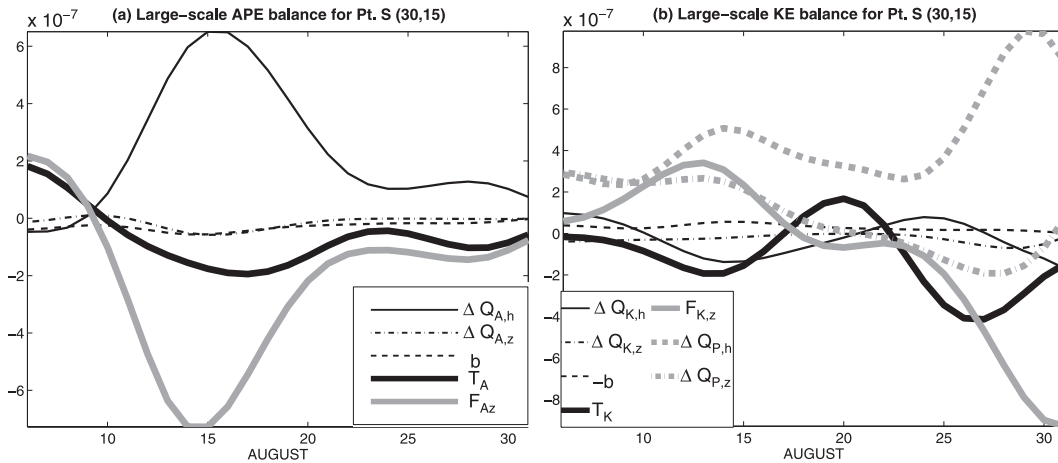


FIG. 19. Large-scale (a) APE and (b) KE balance for point S(30,15) at depth 10 m (cf. Fig. 17 for location). Inserted are the legends for the MS-EVA terms. The symbols are $\Delta Q_{A,h}$ horizontal APE advection; $\Delta Q_{A,z}$ vertical APE advection; b : buoyancy conversion; T_A : total APE transfer; $F_{A,z}$ vertical diffusion; $\Delta Q_{K,h}$ horizontal KE advection; $\Delta Q_{K,z}$ vertical KE advection; $\Delta Q_{P,h}$ horizontal pressure work; $\Delta Q_{P,z}$ vertical pressure work; T_K : total KE transfer; $F_{K,z}$ vertical dissipation; They are the same as listed in Table 1, but with time location index n and window index ϖ removed ($\varpi = 0$ here) for clarity.

center and has established it outside Point Año Nuevo when the wind relaxes.

But the Bay mode KE equation is slightly different: the balance is between horizontal pressure work and the work done by winds together with vertical pressure force. Especially different is the coincidence of the transfers to the external forcing work. In Fig. 20a, $T_{A_n^0}$ almost vanishes when the absolute value of $F_{A_n^0}$ reaches its peak on 14–15 August, while $-T_{A_n^0}$ is maximized as the wind relaxes. A similar scenario is seen in Fig. 20b. The $T_{K_n^0}$ takes its significant negative value from 17 to 25 August, which corresponds to the valley of the curve of $F_{K_n^0}$. Clearly, the instability mode at point B has a driving mechanism completely different from that of point S. It seems to be the relaxation of winds that makes this region unstable.

b. Horizontal MS-EVA maps

Now look at the horizontal maps of the major MS-EVA terms. In Fig. 21, the two most significant terms in the APE balance are contoured for 15 August. Observe the two negative centers on the map of vertical APE diffusion ($F_{A_n^0}$). They correspond well in location to the two instability modes discussed above.

The KE balance is mainly between horizontal pressure working rate $\Delta_h Q_{P_n^0}$, vertical pressure working rate $\Delta_z Q_{P_n^0}$, and the wind working rate $F_{K_n^0}$. From Fig. 20 it is evident that the three are related well to each other. Indeed, this is true in most of the regions at depth 10 m, as seen in Fig. 22. Of particular interest are the two

distinct positive regimes of $F_{K_n^0}$. They are related to the two barotropic transfer centers.

There is a strong negative regime in Fig. 22c (top left corner). Recall that in discussing the large-scale energy distribution (cf. Fig. 13), a large kinetic energy center is identified in this place. Different from the two instability modal centers, one cannot identify a correspondence on the transfer maps. Now it is clear that this kinetic energy patch is highly related to the wind and is therefore not due to intrinsic processes.

To summarize, the large-scale MS-EVA balance is mainly between the external forcing and the advective work together with the pressure work. Both the baroclinic transfer and the barotropic transfer covary with the wind, but the ways they covary in the two distinct transfer centers are quite different. It is evidenced that the Point Sur mode is excited directly by the wind, while the Bay mode is due to a loss of balance established as the wind strengthens. The latter provides an example of

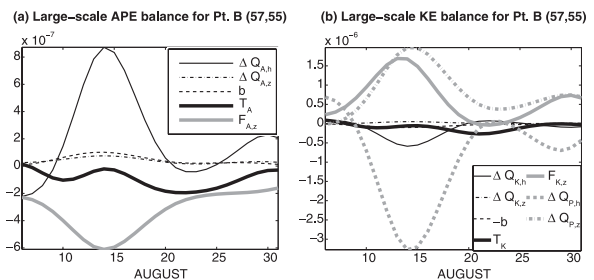


FIG. 20. Same as in Fig. 19, but for point B (57,55).

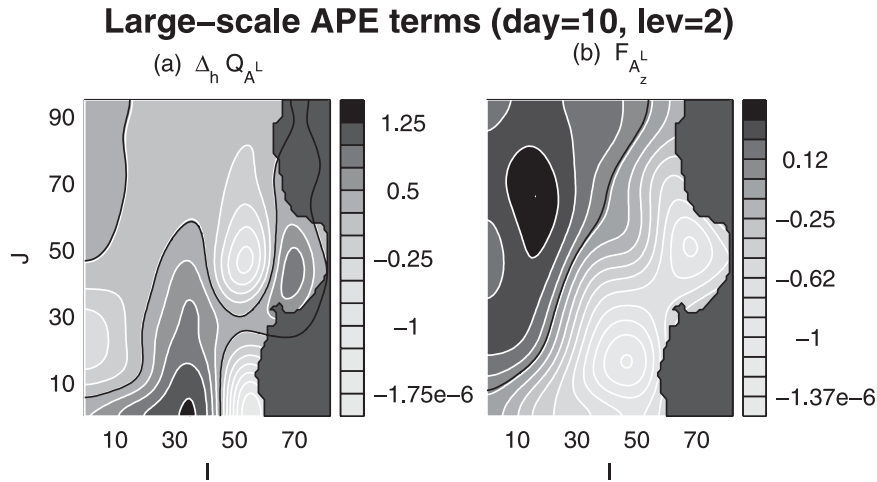


FIG. 21. Large-scale potential energy balance ($\text{m}^2 \text{s}^{-3}$) at the second level (10 m) on 15 August. The zero contour line is plotted in black.

excitation of ocean motion through storing energy first within the large-scale window and then releasing it to form mesoscale processes.

9. Nonlinear internal forcings that drive the temporal submesoscale processes

According to the previous spectral analysis, processes with temporal scales less than a day belong to the submesoscale window. Submesoscale processes are found active for this region. In this study, however, it is difficult to investigate them on the submesoscale window. The original simulation was generated such that observational data are assimilated on a daily basis. Daily processes are interfered by the assimilation scheme, and a direct analysis of the submesoscale energetics therefore could not be reliable. The presence of strong internal tides in this region (Petruncio 1998), which is removed here, poses extra difficulty. Nevertheless, one may still gain some understanding about the submesoscale physics based on the mesoscale window. Particu-

larly, the internal forcings, namely, the perfect transfers that drive the submesoscale processes, can be readily obtained from the mesoscale dynamics.

First we discuss the simple case. In deep layers such as level 12 (150 m), the submesoscale processes are rather weak (not shown). Only a brief description is given here. On the maps of $T_{K_1}^{1 \rightarrow 2}$, the significant transfer occurs in a region just near Point Año Nuevo, particularly after the relaxation. On the $T_{A_n}^{1 \rightarrow 2}$ maps, the transfer is limited within the Bay. Generally speaking, it is positive before 20 August, and after that it becomes negative. Recall that mesoscale thermal structures are generated at this level within the Bay throughout the experiment. The negative $T_{A_n}^{1 \rightarrow 2}$ means that although deriving their energy mainly from the large-scale background, these mesoscale structures after 20 August may also have a partial energy source from the submesoscale processes.

The submesoscale processes on the surface levels are more interesting. Contoured in Fig. 23 is a snapshot of the second-level (10 m) energy transfers from the mesoscale window to the submesoscale window. Both the

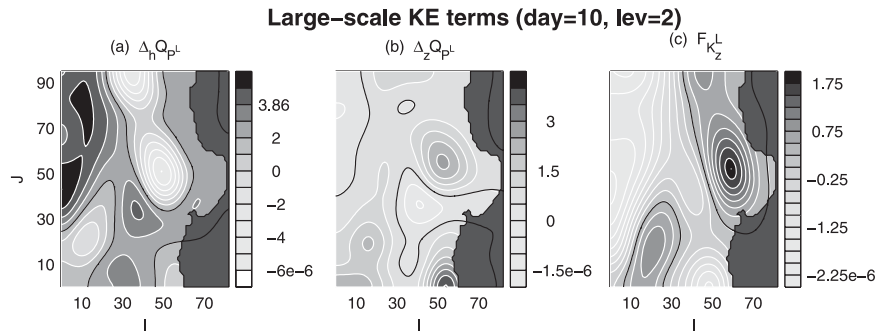


FIG. 22. Large-scale kinetic energy balance ($\text{m}^2 \text{s}^{-3}$) at the second level (10 m) on 15 August. The zero contour line is plotted in black.

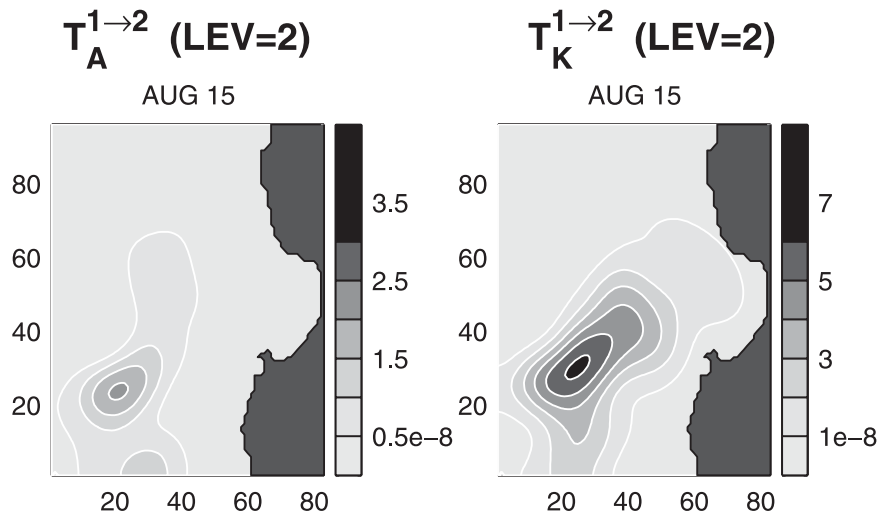


FIG. 23. (left) Potential energy transfer ($\text{m}^2 \text{s}^{-3}$) and (right) kinetic energy transfer ($\text{m}^2 \text{s}^{-3}$) between meso-sub-mesoscale windows on 15 August for depth 10 m. Positive values indicate a transfer from the mesoscale window to the submesoscale window.

(left) APE and (right) KE demonstrate a cascade of energy toward smaller scales on this day (15 August). This trend persists on the KE transfer map as of 21 August, when it becomes more complicated. On the APE transfer map, the distribution is similar, except that a negative center moves in from the southwest when the wind relaxes (not shown).

Compared to Figs. 15, 16, Fig. 23 shows that a secondary instability follows the primary instability between the large-scale and mesoscale windows, releasing energy to submesoscale processes. This secondary instability exhibits itself as a type of mixed baroclinicity and barotropicity. If the day-10 (15 August) pattern is observed closely, one finds the secondary instability actually sitting in a location bridging the Bay mode and the Point Sur mode on the maps of Fig. 16, 15. That is to say, the energetic scenario here may be described as two primary instabilities within the Bay and west of Point Sur, followed by a secondary instability lying in between.

10. Summary and conclusions

The multiscale dynamics of the August 2003 circulation in the Monterey Bay region has been investigated using the multiscale energy and vorticity analysis (MS-EVA) and the MS-EVA-based localized instability theory. The whole system is found to be governed by a bimodal instability structure, with two instabilities at two distinct locations. We have studied how the wind instills energy into the ocean to drive this structure.

The Monterey Bay system is found well organized in space and windowed in (time) scales. It can be roughly classified into two dynamically different types: a surface

type and a deep type. During the experimental period, two regimes have been identified as intrinsic sources of the complicated surface flow system. Represented on the MS-EVA maps, these regimes are two positive centers of baroclinic and barotropic perfect transfers (BC and BT, respectively) from the temporal large-scale window to the temporal mesoscale window as constructed. They are located near the Bay and offshore Point Sur, respectively, and, hence, have been termed the Bay mode and the Point Sur mode for convenience.

The two instability modes in the surface layers have different driving mechanisms lying behind them. It is found that the BC and BT in these two regimes vary in accordance with the wind, but the responses are the opposite. A possible conclusion drawn from this observation is that the bimodal structure may result from the wind, perhaps in cooperation with the coastal geometry. The difference between the two modes is that outside Point Sur the wind seems to destabilize the system directly, while near the Bay, the wind tends to stabilize the southward coastal current, and instability occurs when the external constraint is relaxed.

Corresponding to the energy transfers toward the temporal mesoscale window are the mesoscale fields. The mesoscale temperature and flow are found to be trapped above 200 m during the experiment, with a maximum near the thermocline. The potential and kinetic energy transfers generally correspond in timing to the mesoscale temperature and velocity, respectively, though sometimes discrepancy in location does exist. We observed remarkable cooling during the wind recession on 19 August. It is clearly not driven directly by the wind, nor from a remote region via wave propagation,

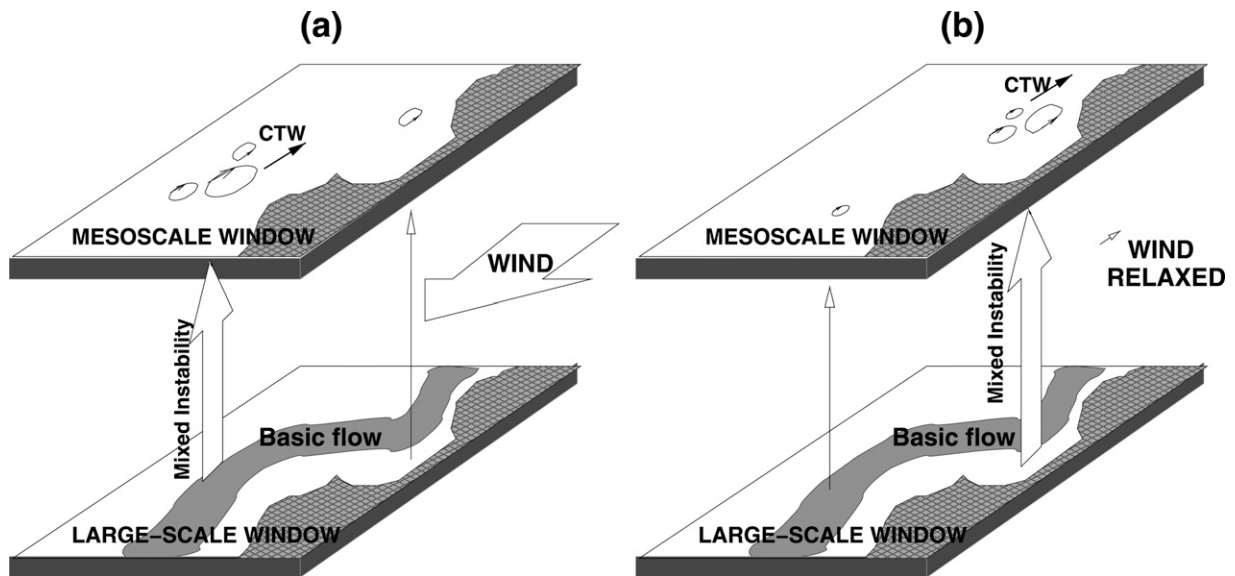


FIG. 24. A cartoon summarizing the major dynamical processes in the upper layer of the Monterey Bay. Two modes of instability, both of mixed type, are identified near the bay and outside Point Sur, respectively. The Point Sur mode (a) is stronger when the southwestward wind applies, while the bay mode (b) results mainly from the relaxation of the wind. The generated mesoscale events propagate northward in the form of coastal trapped waves (CTW).

but rather is caused by the local baroclinic instabilities. It is found that the Bay is a source region of perturbation. Disturbances are generated throughout the experiment, and it seems that the generated disturbances propagate northward along the coast, with a speed close to that of the thermocline-trapped mode of coastal-trapped waves. Figure 24 presents a cartoon summarizing the major physical processes in the surface layer.

The temporal large-scale and mesoscale dynamics for the Monterey Bay circulation have distinct vertical structures. A study has been conducted for the deep flow (below the thermocline), which is dynamically much simpler than its surface counterpart. During the experimental period, the Bay is found baroclinically unstable all the time, which forms the only hotspot on the maps of large-to-mesoscale APE transfer. The corresponding large-to-mesoscale KE transfer is different. The flow is barotropically unstable in the middle of the domain, starting from 11 August through the end of wind relaxation (23 August). To the north is a negative transfer (stable), while to the south is another unstable center just offshore Point Sur. The barotropic unstable center is found to be related to the submarine canyon.

Also examined are the temporal submesoscale processes, based on the information available from the perfect transfers from the mesoscale window to the submesoscale window. During 15 through 21 August, a secondary instability is identified in the surface layer from the clear and simple pattern of meso- to sub-

mesoscale transfer lying between the Bay and the southwestern corner. This pattern holds for both the potential energetics and the kinetic energetics, and the secondary instability is thereby of a mixed type. For the deep flow, a remarkable observation is that near the Bay the transfer is negative after the wind relaxes toward the end of the month. That is to say, the deep layer mesoscale flow is not only fueled by the large-scale flow via instabilities, but also has its source derived from the submesoscale processes.

We close the paper by remarking that this study describes an avenue by which winds can excite the ocean through building up energy in the large-scale background, and then releasing it upon relaxation to energize mesoscale eddies. A sudden cooling in the coastal ocean does not need to be directly driven by the wind, nor a result of remote cooling via wave propagation; it could be driven by a local instability process occurring in situ.

Acknowledgments. The simulation on which this dynamical study is based is the collaborative reanalysis of the AOSN-II August 2003 Monterey Bay circulation performed by the Harvard Ocean Modeling Group, led by Dr. Patrick J. Haley Jr., who provided the Harvard Ocean Prediction System output. We appreciate Wayne Leslie's help with the computing and the buoy and wind data. The authors acknowledge with gratitude the data-gathering efforts of the following scientists during

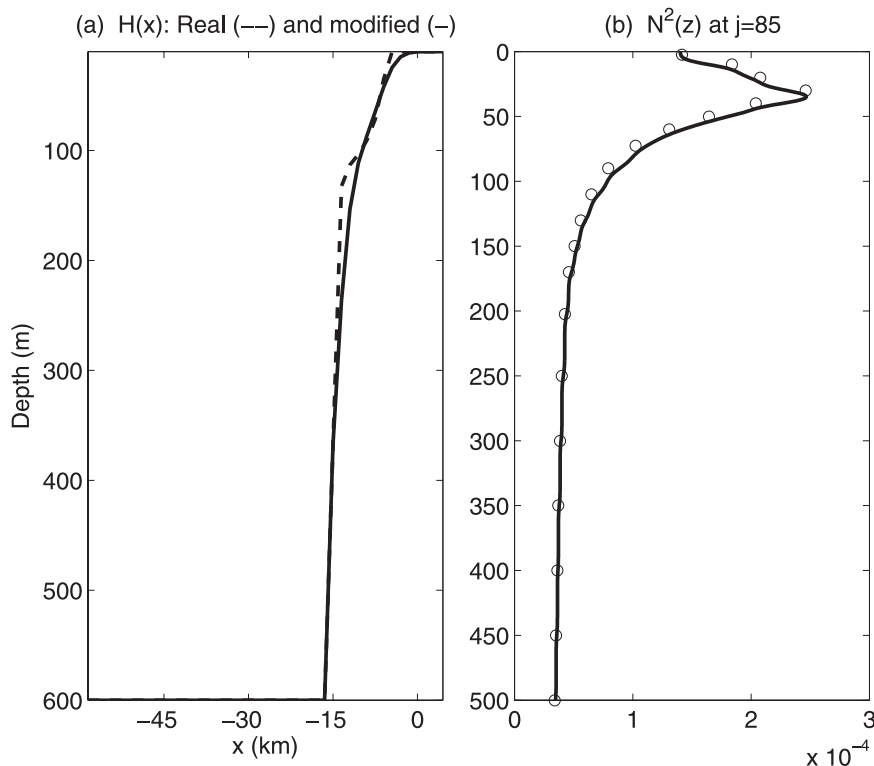


FIG. A1. (a) Topography and (b) buoyancy frequency profiles for the coastal trapped waves computation.

AOSN- II: Dr. Francisco Chavez, Dr. Russ Davis, Dr. David Fratantoni, Dr. Steven Haddock, Dr. Margaret McManus, Dr. Erika McPhee-Shaw, and Dr. Steven Ramp. XSL also thanks Dr. Pierre Lermusiaux for several important discussions on the underlying dynamical processes. Dr. Rucheng Tian read through an early version of this paper, and his remarks are sincerely appreciated. Thanks are due to an anonymous reviewer whose comments helped improve the presentation of material. This work was partially supported by the Office of Naval Research under Grants MURI-ASAP (N00014-04-1-0534) and Dynamics of Oceanic Motions (N00014-02-1-0989) to Harvard University.

APPENDIX

Coastal-Trapped Waves in the Monterey Bay Region

The free coastal-trapped waves in the Monterey Bay region have been studied with three cross-shelf sections. The results are similar. One section is outside Point Año Nuevo, where wave propagations are frequently observed during the AOSN-II experiment. The topography is slightly modified, as marked in Fig. A1a. The basic buoyancy frequency, which is shown in Fig. A1b, is computed from the density profile averaged over all the

available simulated density data on the sections throughout the experiment. The eigenvalue problem is formed and solved with the method by Brink (1980,1991), Clarke and Gorder (1986), and Wilkin and Chapman (1987).

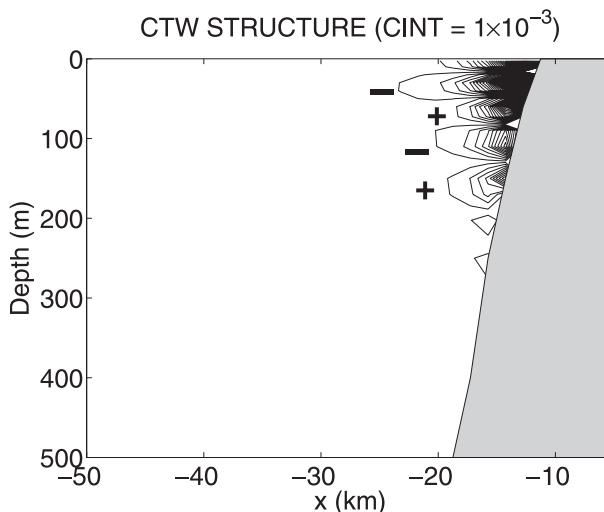


FIG. A2. The structure of the thermocline trapped mode of the coastal trapped waves in the Monterey Bay region. It corresponds to a phase celerity of $c \approx 0.09 \text{ m s}^{-1}$. The signs “+” and “-” indicate the positive and negative regions of contour lines. The contour interval is 1×10^{-3} (units arbitrary).

The eigenfunction of the thermocline-trapped mode is shown in Fig. A2, which corresponds to a phase celerity of 0.09 m s^{-1} .

REFERENCES

- Bigelow, H. B., and M. Leslie, 1930: Reconnaissance of the waters and plankton of Monterey Bay, July, 1928. *Bull. Mus. Comp. Zool.*, **70**, 427–581.
- Breaker, L. C., and C. N. K. Mooers, 1986: Oceanic variability off the central California coast. *Prog. Oceanogr.*, **17**, 61–135.
- , and W. W. Broenkow, 1994: The circulation of Monterey Bay and related processes. *Oceanography and Marine Biology: An Annual Review*, A. D. Ansell, R. N. Gibson, and M. Barnes, Eds., Vol. 32, UCL Press, 1–64.
- Brink, K. H., 1980: Propagation of barotropic continental shelf waves over irregular bottom topography. *J. Phys. Oceanogr.*, **10**, 765–778.
- , 1991: Coastal-trapped waves and wind-driven currents over the continental shelf. *Annu. Rev. Fluid Mech.*, **23**, 389–412.
- , and T. J. Cowles, 1991: The Coastal Transition Zone Program. *J. Geophys. Res.*, **96**, 14 637–14647.
- Chelton, D. B., A. Bratkovch, R. L. Bernstein, and P. M. Kosro, 1988: The poleward flow off central California during the spring and summer of 1984. *J. Geophys. Res.*, **93**, 10 604–10 620.
- Clarke, A., and V. Gorder, 1986: A method for estimating wind-driven frictional, time-dependent, and stratified shelf and slope water flow. *J. Phys. Oceanogr.*, **16**, 1013–1028.
- Collins, C. A., N. Garfield, T. A. Rago, F. W. Rischmiller, and E. Carter, 2000: Mean structure of the inshore countercurrent and California undercurrent off Point Sur, California. *Deep-Sea Res. II*, **47**, 765–782.
- Dewery, R. K., J. N. Moum, C. A. Paulson, D. R. Caldwell, and S. D. Pierce, 1991: Structure and dynamics of a coastal filament. *J. Geophys. Res.*, **96**, 14 885–14 907.
- Griggs, G. B., 1974: Nearshore current patterns along the central California coast. *Estuaries Coastal Mar. Sci.*, **2**, 395–405.
- Haley, P. J., and Coauthors, 2008: Forecasting and reanalysis in the Monterey Bay/California Current region for the autonomous ocean sampling network-II experiment. *Deep-Sea Res. II*, (Special Issue), doi:10.1016/j.dsr2.2008.08.010.
- Hickey, B. M., 1998: Coastal oceanography of western North America from the tip of Baja California to Vancouver Island. *The Sea*, A. R. Robinson and K. H. Brink, Eds., Vol. 12, Wiley, 345–393.
- Kelly, K. A., 1985: The influence of winds and topography on the sea surface temperature patterns over the northern California slope. *J. Geophys. Res.*, **90**, 1655–1681.
- Lermusiaux, P. F. J., 2007: Adaptive modeling, adaptive data assimilation and adaptive sampling. *Physica D*, **230**, 172–196.
- Li, Z., Y. Chao, J. C. McWilliams, and K. Ide, 2008: A three-dimensional variational data assimilation scheme for the regional ocean modeling system: Implementation and basic experiments. *J. Geophys. Res.*, **113**, C05002, doi:10.1029/2006JC004042.
- Liang, X. S., and A. R. Robinson, 2004: A study of the Iceland–Faeroe frontal variability using the multiscale energy and vorticity analysis. *J. Phys. Oceanogr.*, **34**, 2571–2591.
- , and M. Wang, 2004: A study of turbulent wakes using a novel localized stability analysis. *Proc. Center for Turbulence Research Summer Program 2004*, Stanford, CA, Stanford–NASA Ames Research Center, 211–222.
- , and A. R. Robinson, 2005: Localized multiscale energy and vorticity analysis. I. Fundamentals. *Dyn. Atmos. Oceans*, **38**, 195–230.
- , and D. G. M. Anderson, 2007: Multiscale window transform. *SIAM J. Multiscale Model. Simul.*, **6**, 437–467.
- , and A. R. Robinson, 2007: Localized multi-scale energy and vorticity analysis. II. Theory of finite-amplitude instability. *Dyn. Atmos. Oceans*, **44**, 51–76, doi:10.1016/j.dynatmoce.2007.04.001.
- Lipphardt, B. L., Jr., D. Small, A. D. Kirwan Jr., S. Wiggins, K. Ide, C. E. Grosch, and J. D. Paduan, 2006: Synoptic Lagrangian maps: Application to surface transport in Monterey Bay. *J. Mar. Res.*, **64**, 221–247.
- Liu, Y., X. S. Liang, and R. H. Weisberg, 2007: Rectification of the bias in the wavelet power spectrum. *J. Atmos. Oceanic Technol.*, **24**, 2093–2102.
- Miller, A. J., and Coauthors, 1999: Observing and modeling the California Current System: Purposes, achievements and aspirations. *Eos, Trans. Amer. Geophys. Union*, **80**, 533–539.
- Narimousa, S., and T. Maxworthy, 1989: Application of a laboratory model to the interpretation of satellite and field observations of coastal upwelling. *Dyn. Atmos. Oceans*, **13**, 1–46.
- Petruncio, E. T., 1998: Observations of the internal tide in Monterey Canyon. *J. Phys. Oceanogr.*, **28**, 1873–1903.
- Ramp, S. R., L. K. Rosenfeld, T. D. Tisch, and M. R. Hicks, 1997: Moored observations of the current and temperature structure over the continental slope off central California. 1. A basic description of the variability. *J. Geophys. Res.*, **102**, 22 877–22 902.
- , and Coauthors, 2008: Preparing to predict: The second Autonomous Ocean Sampling Network (AOSN-II) experiment in the Monterey Bay. *Deep-Sea Res. II* (Special Issue), in press.
- Rosenfeld, L. K., F. B. Schwing, N. Garfield, and D. E. Tracy, 1994: Bifurcation flow from an upwelling center: A cold water source for Monterey Bay. *Cont. Shelf Res.*, **14**, 931–964.
- Shepard, F. P., R. Revelle, and R. S. Dietz, 1939: Ocean-bottom currents off the California coast. *Science*, **89**, 488–489.
- Skogsberg, T., 1936: *Hydrography of Monterey Bay, California: Thermal conditions, 1929–1933*. Transactions of the American Philosophical Society, Vol. 29, American Philosophical Society, 152 pp.
- Strang, G., and T. Nguyen, 1996: *Wavelets and Filter Banks*. Wellesley-Cambridge Press, 520 pp.
- Strub, P. T., J. S. Allen, A. Huyer, and R. L. Smith, 1987: Seasonal cycles of currents, temperatures, winds, and sea level over the northeast Pacific continental shelf: 35°N to 48°N. *J. Geophys. Res.*, **92**, 1507–1526.
- Wilkin, J. L., and D. C. Chapman, 1987: Scattering of continental shelf waves at a discontinuity in shelf width. *J. Phys. Oceanogr.*, **17**, 713–724.
- Xie, L., X. Liu, and L. J. Pietrafesa, 2007: Effect of bathymetric curvature on Gulf Stream instability in the vicinity of the Charleston Bump. *J. Phys. Oceanogr.*, **37**, 452–475.